



저작자표시-비영리-변경금지 2.0 대한민국

이용자는 아래의 조건을 따르는 경우에 한하여 자유롭게

- 이 저작물을 복제, 배포, 전송, 전시, 공연 및 방송할 수 있습니다.

다음과 같은 조건을 따라야 합니다:



저작자표시. 귀하는 원저작자를 표시하여야 합니다.



비영리. 귀하는 이 저작물을 영리 목적으로 이용할 수 없습니다.



변경금지. 귀하는 이 저작물을 개작, 변형 또는 가공할 수 없습니다.

- 귀하는, 이 저작물의 재이용이나 배포의 경우, 이 저작물에 적용된 이용허락조건을 명확하게 나타내어야 합니다.
- 저작권자로부터 별도의 허가를 받으면 이러한 조건들은 적용되지 않습니다.

저작권법에 따른 이용자의 권리는 위의 내용에 의하여 영향을 받지 않습니다.

이것은 [이용허락규약\(Legal Code\)](#)을 이해하기 쉽게 요약한 것입니다.

[Disclaimer](#)

이학박사학위논문

Mechanical and electronic properties of
graphene under extrinsic conditions

외부 환경 아래에 놓인 그래핀의
역학적 성질과 전자적 성질

2016년 2월

서울대학교 대학원
물리천문학부
황 정 은

Mechanical and electronic properties of graphene under extrinsic conditions

Jeongwoon Hwang

Supervised by

Professor **Jisoon Ihm**

A Dissertation

Submitted to the Faculty of

Seoul National University

in Partial Fulfillment of

the Requirements for the Degree of

Doctor of Philosophy

December 2015

Department of Physics and Astronomy

The Graduate School

Seoul National University

Abstract

Mechanical and electronic properties of graphene under extrinsic conditions

Jeongwoon Hwang

Department of Physics and Astronomy

The Graduate School

Seoul National University

Since the groundbreaking experiments in 2004, the following years have been the era of graphene, a two-dimensional material. Graphene has been an exciting playground for both theorists and experimentalists due to its two-dimensional nature and the fascinating material properties. Although many theoretical studies have been performed on the ideal form of graphene in the limit of an infinite lattice, in real experimental situations, however, what we encounter are apart from those theoretically expected from the ideal graphene. Therefore, aside from revealing the intrinsic properties of graphene, it is also important to expect the changes of its properties under extrinsic conditions. Meanwhile, those deviations may come from the existence of edge or boundary, the substrate-induced stress, and the electronic hybridization with substrates. An encounter with edge or boundary is inevitable

in real situations, but there is a still room for refining it. Moreover, a removal of the substrate-induced degradation and an improvement of experimental environments can be achieved by choosing the right substrates.

With those facts in mind, in this thesis we focus on the mechanical and electronic properties of graphene under extrinsic conditions. In the first part, mechanical properties of graphene under general tensile strain are studied. *Ab initio* force constant method is adopted to calculate phonon dispersions with the usual first-principles calculations. We show the transition of Kohn anomaly points from a high-symmetry k point to a lower-symmetry one under the symmetry-lowering tensile strain, which can be interpreted in relationship to the Dirac point shift in the electronic structure. We demonstrate that the strain-induced enhancement of phonon softening can give rise to phonon instabilities over a wide range of tensile strain directions, resulting in a mechanical failure of graphene at lower strains. In addition, we show that there are two types of instabilities leading to mechanical failure prior to the elastic failure. In the second part, electronic properties of epitaxially grown graphene/hexagonal boron nitride double layer are studied in regard to a scanning tunneling microscopy experiment. Scanning tunneling microscopy simulations based on first-principles calculations are performed to identify the sample on which the measurements were conducted in the experi-

ment. We demonstrate the limitation of such measurement on graphene directly contacting with metal substrates. We also clarify the role of hexagonal boron nitride monolayer in the system by showing the differences in the projected density of states and decaying patterns of charge densities with and without the layer. In addition, we investigate the zigzag edge localized state of graphene on *h*-BN monolayer with low-energy effective Hamiltonian and reproduce the experimental results. Finally, we summarize this thesis and present perspectives for further exploration.

Keywords: graphene, Kohn anomaly, phonon instability, graphene hexagonal boron nitride double layer, scanning tunneling microscopy simulation, zigzag edged graphene

Student Number: 2009-20435

Contents

Abstract	i
I. Introduction	1
II. Tight-binding description of graphene and zigzag graphene nanoribbon	5
2.1 Basics	5
2.2 Tight-binding model description of graphene	7
2.3 Hubbard model description of zigzag graphene nanoribbons	13
III. Computational methods	17
3.1 Density functional theory	17
3.1.1 Hohenberg-Kohn theorem	18
3.1.2 Kohn-Sham formulation	21
3.1.3 Approximations for exchange-correlation energy	25
3.2 Pseudopotential plane wave approach	31
3.2.1 Plane wave basis set	31
3.2.2 Pseudopotential theory	34
3.2.3 Projector augmented method	41

3.3	Van der Waals interaction	43
3.4	<i>Ab initio</i> force constant methods	45
IV. Phonon softening and mechanical failure of graphene		
	under tensile strain	51
4.1	Introduction	52
4.2	Calculation details	58
4.3	Results and discussion	58
4.3.1	Symmetry lowering strains and transition of phonon softening points	58
4.3.2	Crossover between two phonon instabilities .	61
4.3.3	Phonon instability-driven mechanical failure .	64
4.4	Conclusion	69
V. Investigation of graphene/hexagonal boron nitride dou-		
	ble layer in regard to an STM experiment	71
5.1	Introduction	71
5.2	Calculation details	75
5.3	Results and discussion	77
5.3.1	Effect of substrates on STM simulation . . .	77
5.3.2	Study of localized states at graphene zigzag edge	83
5.4	Conclusion	87

VI. Summary and perspectives	89
Bibliography	91
국문초록	103

List of Figures

2.1	(a) Atomic structure of graphene. $\mathbf{a}_{i=1,2}$ denote real space lattice vectors. $\boldsymbol{\tau}_{i=1,2,3}$ are hopping vectors connecting nearest neighbor carbon atoms on two sublattices, A and B. (b) First Brillouin zone of graphene. $\mathbf{b}_{i=1,2}$ denote reciprocal lattice vectors. There are two inequivalent Dirac points at K and K'	6
2.2	Zigzag graphene nanoribbon. \mathbf{a} denotes a lattice vector along which the system has 1D translational symmetry. Up and down arrows with circle at both edges are drawn to emphasize spin-polarized edge states.	14
2.3	Tight-binding band structures of 8 zigzag graphene nanoribbon with and without on-site repulsion term. For finite U, band gap opens.	16
4.1	(a) Primitive cell and the first Brillouin zone (BZ) of graphene. The irreducible BZ (IBZ) is represented by the shaded area in red. (b),(c) Atomic structures and BZs of graphene under the Z- and A-strain, respectively. The direction of the Z (A)-strain is in parallel with the x (y)-axis. The IBZ is expanded from triangle to trapezoid due to the symmetry lowering strain. . . .	56

4.2 (a) BZs of electron (left) and phonon (right), respectively, under the Z-strain and (b) the same for the A-strain. In the left figures of (a) and (b), green arrows represent Dirac points shift, and red arrows are vectors connecting two Dirac points. Blue arrows in the right figures of (a) and (b) represent the positions of the frequency dips (wave vector of the soft phonon) in the phonon dispersion. (c),(d) Phonon band structures under the Z- and A-strain, respectively (plotted along purple lines in (a) and (b)). Different colors indicate different strain configurations (see inset). Phonon softening points gradually move away from K (K') and corresponding phonon frequencies are lowered as the Z (A)-strain increases. 59

4.3 Crossover between the near Γ -softening and the K-anomaly. (a) Phonon band structures at $(e_x, e_y) = (0.193, 0.05)$ and $(0.218, 0.05)$ for left and right figures, respectively. The near Γ -softening (red arrow) occurs earlier than the K-anomaly. (b) Phonon band structures at $(e_x, e_y) = (0.184, 0.11)$ and $(0.194, 0.11)$ for left and right figures, respectively. The K-anomaly (black arrow) occurs before the near Γ -softening. 62

4.4	(a) Phonon instability-driven distortion occurring at the onset strain of (13.33%, 20%) and (b) the corresponding total energy and stress relation with varying displacement amplitude under the same tensile strain. (c) Phonon instability-driven distortion occurring at the onset strain of (17%, 14.17%) and (d) the stress-strain relation above the onset strain.	65
4.5	(a),(b) Distorted structures induced by the K-anomalies under a Z-strain (13.33%, 20%) and an A-strain (17%, 14.17%), respectively. (c) Distorted structure induced by the near Γ -softening under an A-strain (19.84%, 7%). The K-anomaly induced structures show local hexagonal clustering, while the near Γ -softening induces bond elongation along one direction.	67
5.1	Atomic configurations of (a) graphene monolayer, (b) graphene/ <i>h</i> -BN double layer, and (c) <i>h</i> -BN monolayer over six atomic-layer of Cu(111) substrate for STM simulations. Here, we explicitly consider various substrates in the calculations. STM simulation is schematically drawn in (d), where a purple trapezoid represents the STM tip.	77

5.2 Calculated charge densities of (a) graphene on Cu(111) at 4 Å away, (b) graphene on *h*-BN/Cu(111) at 3 Å away, and (c) *h*-BN on Cu(111) at 4 Å away, where *h* denotes the center of a hexagon. (d) $(1.6 \times 1.6) \text{ nm}^2$ STM topography of graphene monolayer on *h*-BN. A simulated image is shown in the bottom right corner. (e) Tunneling spectra along the zigzag edge at locations A, B, C, D, E, and F in (d). These spectra overlap nicely, showing reproducibility. (f) Difference spectra, dI/dV subtracted from the bulk dI/dV , obtained at locations 1, 2, 3, 4, 5, and 6 in (d). 79

5.3 Projected density of states onto (a) C p-orbital, (b) Cu s-orbital, and (c) B p-orbital near Fermi energy, respectively. Calculated charge densities in the direction of surface normal are shown in (d) for the marked states in (a), (e) for those in (b), and (f) for those in (c), in log scale. Electronic states in the range of $\pm 25 \text{ meV}$ of marked peaks are integrated for calculating charge densities. Without insulating *h*-BN layer, Cu s-orbital dominant state decays very slowly showing its tail above the graphene layer in (d). 82

5.4 (a) Tight-binding band structures of 100-ZGNR. Depending on whether on-site Coulomb repulsion terms are considered only at the zigzag edges or at all carbon sites, the edge state becomes conducting (the left panel) or semiconducting (the right panel). (b) Calculated LDOS at the zigzag edge, which reproduces well STS data measured on the zigzag edge in Figure 5.2(f). 86

Chapter 1

Introduction

Graphene is a monolayer of carbon atoms on two-dimensional honeycomb lattice and is a basic building block for all other graphitic materials of various dimensionalities [1]. Thorough theoretical studies of graphene for decades had been followed by the finding of free-standing graphene [2] which literally has opened the era of graphene. Interestingly, the existence of such a two-dimensional crystalline structure at finite temperature is not inconsistent with the Mermin's theorem [3] by virtue of gentle crumpling in the third dimension.

Graphene shows truly fascinating properties: it is the strongest material ever tested in nature with the Young's modulus of 1 TPa [4] and has exceptional intrinsic electron mobility of $2 \cdot 10^5 \text{ cm}^2 \text{ V}^{-1} \text{ s}^{-1}$ (at a carrier density of $1 \cdot 10^{12} \text{ cm}^{-2}$) due to the ballistic transport on the submicrometer scale [5], which exceeds that of any known semiconductor and is independent of the doping concentration [6]. Theoretically, the low-energy charge carriers of graphene mimic relativistic particles and can naturally be described by the relativistic Dirac equation rather than the usual Schrödinger equation, though the electrons moving around the carbon atoms are not particularly rela-

tivistic. Now experimental discovery of graphene provides a way to probe (2+1)-dimensional quantum electrodynamics phenomena [7–9]. Therefore, graphene has fascinated theorists and experimentalists alike.

With the rise of graphene, there have been various experimental attempts to produce graphene of high-quality and large-area, which include chemical exfoliation [10], mechanical exfoliation of graphite on SiO_2/Si [2], thermal graphitization of a silicon carbide surface [11], reduction from graphite oxide [12], and chemical vapor deposition of hydrocarbons on metal substrates [13]. Obviously, the experimentally measured properties of graphene are under the influence of the sample quality, which may be affected by impurities, defects, ripples, grain boundaries, and reconstructions at the edges. The environmental factors such as interaction with a substrate also have been reported to change the characteristics of graphene [6, 14]. These deviations from ideal graphene modify or degrade the expected performance of graphene.

In this thesis, first-principles calculations and tight-binding analysis have been performed concerning the properties of graphene under extrinsic conditions, i.e., the externally applied mechanical stress and the electronic perturbation from substrates. In chapter 2, we briefly review basic theoretical models for describing graphene and graphene nanoribbons. In chapter 3, modern density functional theory (DFT)

is introduced, where the fundamental theorem of DFT, Kohn-Sham formulation, exchange-correlation functionals, and the pseudopotential method with plane wave basis set are explained. We also present *ab initio* force constant method for phonon dispersion calculation. In chapter 4, the mechanical properties of strained graphene and its failure mechanism are studied by DFT calculations with the aforementioned phonon calculation method. In chapter 5, electronic properties of epitaxially grown graphene/hexagonal boron nitride double layer on the Cu(111) substrate are studied by DFT calculations and the low-energy effective Hamiltonian, in regard to a scanning tunneling microscopy experiment. We conclude with a brief summary of this work and perspectives for future work in chapter 6.

Chapter 2

Tight-binding description of graphene and zigzag graphene nanoribbon

In this chapter, we introduce the tight-binding model for graphene to describe the low-energy electronic structure near the charge neutral point. For graphene with the parallel zigzag edges, the localized electronic states exist at both edges, which can be described by the Hubbard model Hamiltonian. The Hubbard model Hamiltonian is composed of hopping term and on-site repulsion term, which explicitly deals with the electron-electron interaction, and without on-site repulsion term it simply becomes the tight-binding model.

2.1 Basics

Graphene is a two-dimensional hexagonal lattice system of carbon atoms with a basis of two atoms per unit cell, which has D_{6h} point group symmetry. The primitive lattice vectors of graphene can be written as

$$\mathbf{a}_1 = \sqrt{3}a\left(\frac{\sqrt{3}}{2}, -\frac{1}{2}\right), \quad \mathbf{a}_2 = \sqrt{3}a\left(\frac{\sqrt{3}}{2}, \frac{1}{2}\right), \quad (2.1)$$

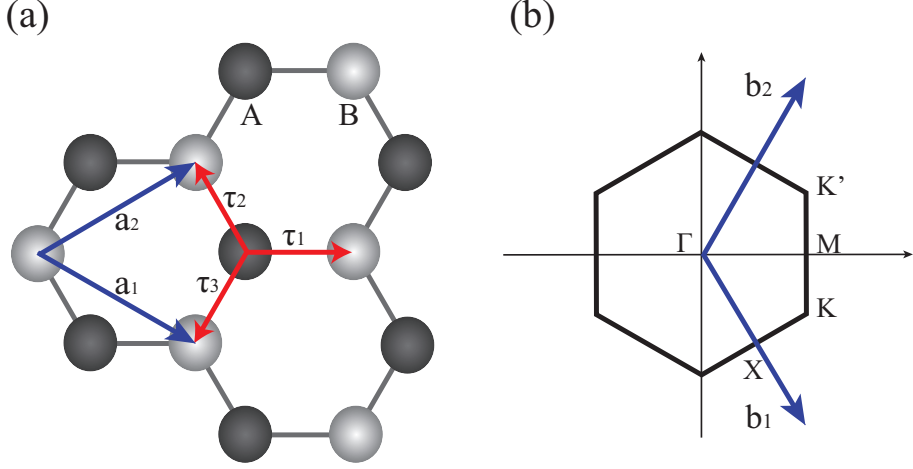


Figure 2.1: (a) Atomic structure of graphene. $\mathbf{a}_{i=1,2}$ denote real space lattice vectors. $\boldsymbol{\tau}_{i=1,2,3}$ are hopping vectors connecting nearest neighbor carbon atoms on two sublattices, A and B. (b) First Brillouin zone of graphene. $\mathbf{b}_{i=1,2}$ denote reciprocal lattice vectors. There are two inequivalent Dirac points at K and K'.

where the nearest carbon-carbon distance is $a \approx 1.42 \text{ \AA}$. The corresponding reciprocal lattice vectors are

$$\mathbf{b}_1 = \frac{4\pi}{3a} \left(\frac{1}{2}, -\frac{\sqrt{3}}{2} \right), \quad \mathbf{b}_2 = \frac{4\pi}{3a} \left(\frac{1}{2}, \frac{\sqrt{3}}{2} \right). \quad (2.2)$$

There are two inequivalent zone corners K and K' of the Brillouin zone,

$$\mathbf{K} = \frac{2\pi}{3a} \left(1, -\frac{1}{\sqrt{3}} \right), \quad \mathbf{K}' = \frac{2\pi}{3a} \left(1, \frac{1}{\sqrt{3}} \right), \quad (2.3)$$

where the energy band structure shows linear dispersion near Fermi energy with zero energy gap. The low-energy quasiparticles near these two points can formally be described by the Dirac-like Hamiltonian, and thus K and K' are called Dirac points.

2.2 Tight-binding model description of graphene

The energy bands near the Fermi energy determine the low-energy properties of the system, which is of great interest in this section. This low-energy bands can be obtained by solving a tight-binding Hamiltonian, where the basis functions are linear combinations of p_z atomic orbitals on two sublattices, i.e. $\varphi_A(\mathbf{r} - \mathbf{R} - \tau_A)$ and $\varphi_B(\mathbf{r} - \mathbf{R} - \tau_B)$, where \mathbf{R} is a unit cell index, and $\tau_{A,B}$ denote the positions of carbon atoms on A and B sublattices in a unit cell. Since there are two p_z orbitals per unit cell, we get upper and lower bands near Fermi energy which touch each other at the Dirac points. The spin degrees of freedom can be ignored at present because graphene has non-magnetic ground state. The basis functions can be written in the Bloch form,

$$\phi_{\alpha k}(\mathbf{r}) = \frac{1}{\sqrt{N}} \sum_{\mathbf{R}} e^{i\mathbf{k} \cdot (\mathbf{R} + \tau_{\alpha})} \varphi_{\alpha}(\mathbf{r} - \mathbf{R} - \tau_{\alpha}), \quad (2.4)$$

where two sublattices (A and B) are designated by α and N is the number of unit cells in the crystal. Then we need to solve the eigen-

value problem

$$H\Psi_{nk} = E_{nk}\Psi_{nk}, \quad (2.5)$$

where the Hamiltonian of the system is given by

$$H = \frac{p^2}{2m} + V(\mathbf{r}) + \sum_{R \neq 0} V(\mathbf{r} - \mathbf{R}) \quad (2.6)$$

$$= H_{atom} + \Delta V, \quad (2.7)$$

and eigenstates can be written as

$$\Psi_{nk}(\mathbf{r}) = \sum_{\alpha} c_{\alpha nk} \phi_{\alpha k}(\mathbf{r}). \quad (2.8)$$

If we apply $\phi_{\beta k}$ on both sides of eq. (2.5), it becomes generalized eigenvalue problem of the 2×2 Hamiltonian matrix due to the translation symmetry

$$\sum_{\alpha} H_{\beta\alpha}(\mathbf{k}) c_{\alpha nk} = E_{nk} \sum_{\alpha} S_{\beta\alpha}(\mathbf{k}) c_{\alpha nk}, \quad (2.9)$$

where

$$H_{\alpha\beta}(\mathbf{k}) = \langle \phi_{\alpha k} | H | \phi_{\beta k} \rangle \quad (2.10)$$

$$= \sum_{\mathbf{R}} \int d\mathbf{r} e^{i\mathbf{k} \cdot (\mathbf{R} + \tau_{\beta} - \tau_{\alpha})} \phi_{\alpha}^*(\mathbf{r} - \tau_{\alpha}) H \phi_{\beta}(\mathbf{r} - \mathbf{R} - \tau_{\beta}) \quad (2.11)$$

$$= \sum_{\mathbf{R}} e^{i\mathbf{k} \cdot (\mathbf{R} + \tau_{\beta} - \tau_{\alpha})} (\epsilon_{\alpha} s_{\alpha\beta}(\mathbf{R}) + h_{\alpha\beta}(\mathbf{R})) \quad (2.12)$$

and

$$S_{\alpha\beta}(\mathbf{k}) = \langle \phi_{\alpha k} | \phi_{\beta k} \rangle \quad (2.13)$$

$$= \sum_{\mathbf{R}} e^{i\mathbf{k} \cdot (\mathbf{R} + \tau_{\beta} - \tau_{\alpha})} s_{\alpha\beta}(\mathbf{R}). \quad (2.14)$$

ϵ_{α} denotes the atomic energy of ϕ_{α} , and

$$s_{\alpha\beta}(\mathbf{R}) = \int d\mathbf{r} e^{i\mathbf{k} \cdot (\mathbf{R} + \tau_{\beta} - \tau_{\alpha})} \phi_{\alpha}^*(\mathbf{r} - \tau_{\alpha}) H_{atom} \phi_{\beta}(\mathbf{r} - \mathbf{R} - \tau_{\beta}), \quad (2.15)$$

$$h_{\alpha\beta}(\mathbf{R}) = \int d\mathbf{r} e^{i\mathbf{k} \cdot (\mathbf{R} + \tau_{\beta} - \tau_{\alpha})} \phi_{\alpha}^*(\mathbf{r} - \tau_{\alpha}) \Delta V \phi_{\beta}(\mathbf{r} - \mathbf{R} - \tau_{\beta}) \quad (2.16)$$

Here, $h_{\alpha\beta}(\mathbf{R})$ is the so-called hopping integral representing the energy gain from electron hopping between two atomic orbitals. Solving eigenvalue problem leads to the following secular equation for each \mathbf{k}

$$\sum_{\beta} [H_{\alpha\beta}(\mathbf{k}) - E_{nk} S_{\alpha\beta}(\mathbf{k})] c_{\beta nk} = 0. \quad (2.17)$$

If we consider only the nearest neighbor hopping, i.e.

$$h_{\alpha\beta}(\mathbf{R}) = \begin{cases} t, & \text{if } |\mathbf{R} + \tau_\beta - \tau_\alpha| = |\tau_\beta - \tau_\alpha|, \\ 0, & \text{otherwise,} \end{cases} \quad (2.18)$$

and if the overlap matrix ($S_{\alpha\beta}(\mathbf{k})$) can be approximated as an identity matrix and the on-site energy is set to be zero, we arrive at a simple secular equation of the form

$$\begin{vmatrix} -E(\mathbf{k}) & H_{AB}(\mathbf{k}) \\ H_{BA}(\mathbf{k}) & -E(\mathbf{k}) \end{vmatrix} = 0, \quad (2.19)$$

where

$$H_{AB}(\mathbf{k}) = t \sum_{i=1}^3 e^{i\mathbf{k}\cdot\tau_i} \quad (2.20)$$

$$= t \left[e^{-ik_x a} + 2e^{i\frac{1}{2}k_x a} \cos\left(\frac{\sqrt{3}}{2}k_y a\right) \right], \quad (2.21)$$

and

$$H_{BA}(\mathbf{k}) = H_{AB}^*(\mathbf{k}). \quad (2.22)$$

In the vicinity of a Dirac point ($\mathbf{k} = \mathbf{K} + \mathbf{q}$, $\mathbf{K} = (0, \frac{4\pi}{3\sqrt{3}a})$), the Hamiltonian matrix becomes

$$H(\mathbf{K} + \mathbf{q}) = \begin{pmatrix} 0 & -i\frac{3}{2}ta(q_x - iq_y) \\ i\frac{3}{2}ta(q_x + iq_y) & 0 \end{pmatrix}. \quad (2.23)$$

By unitary transformation $UHU^\dagger = \tilde{H}$, (2.23) becomes a familiar expression

$$H(\mathbf{K} + \mathbf{q}) = \begin{pmatrix} 0 & \frac{3}{2}ta(q_x - iq_y) \\ \frac{3}{2}ta(q_x + iq_y) & 0 \end{pmatrix}, \quad (2.24)$$

where the unitary matrix is given by

$$U = \begin{pmatrix} e^{i\frac{\pi}{4}} & 0 \\ 0 & e^{-i\frac{\pi}{4}} \end{pmatrix} = \exp\left(-\frac{i\sigma_z(-\frac{\pi}{2})}{2}\right), \quad (2.25)$$

which acts on a two-component spinor, or pseudospin, and results in a rotation by $-\frac{\pi}{2}$ about the z-axis. Similarly, we can obtain the expression for $H(\mathbf{K}' + \mathbf{q}) = H^*(\mathbf{K} + \mathbf{q})$. Solving the secular equation leads to eigenvalues

$$E_{K,K'}(\mathbf{q}) = \pm \frac{3}{2}ta|\mathbf{q}| + O\left(\left(\frac{q}{K}\right)^2\right), \quad (2.26)$$

and eigenstates

$$\Psi_{\pm,K}(\mathbf{q}) = \frac{1}{\sqrt{2}} \begin{pmatrix} e^{-i\theta_{\mathbf{q}}/2} \\ \pm e^{i\theta_{\mathbf{q}}/2} \end{pmatrix}, \quad (2.27)$$

$$\Psi_{\pm,K'}(\mathbf{q}) = \frac{1}{\sqrt{2}} \begin{pmatrix} e^{i\theta_{\mathbf{q}}/2} \\ \pm e^{-i\theta_{\mathbf{q}}/2} \end{pmatrix}, \quad (2.28)$$

where $\frac{3}{2}ta = v_F$ is the Fermi velocity, and $\theta_{\mathbf{q}} = \tan^{-1}(q_y/q_x)$.

Now consider the tight-binding Hamiltonian in the second quantization form, which is useful for introducing Hubbard model Hamiltonian in the next section and is given by

$$\hat{H} = t \sum_{\langle i,j \rangle} \left(\hat{a}_i^\dagger \hat{b}_j + \hat{b}_j^\dagger \hat{a}_i \right). \quad (2.29)$$

Here, t is the hopping integral between nearest neighbor carbon p_z orbitals as defined before and $\langle i, j \rangle$ denotes pairs of nearest neighbor atoms. By Fourier transformation of field operators

$$\hat{a}_i^\dagger = \frac{1}{\sqrt{N}} \sum_{\mathbf{k}} \hat{a}_{\mathbf{k}}^\dagger e^{i\mathbf{k} \cdot \mathbf{r}_i}, \quad (2.30)$$

$$\hat{b}_j = \frac{1}{\sqrt{N}} \sum_{\mathbf{k}} \hat{b}_{\mathbf{k}} e^{-i\mathbf{k} \cdot \mathbf{r}_j}, \quad (2.31)$$

we encounter the 2x2 tight-binding Hamiltonian matrix again, where eigenstate is given by

$$|\Psi_{\pm, \mathbf{k}}\rangle = \left(c_{A\pm, \mathbf{k}} \hat{a}_{\mathbf{k}}^{\dagger} + c_{B\pm, \mathbf{k}} \hat{b}_{\mathbf{k}}^{\dagger} \right) |0\rangle. \quad (2.32)$$

In the vicinity of \mathbf{K} , $(c_{A\pm}, c_{B\pm})$ becomes $\frac{1}{\sqrt{2}} \left(e^{-i\theta_{\mathbf{q}}/2}, \pm e^{i\theta_{\mathbf{q}}/2} \right)$.

2.3 Hubbard model description of zigzag graphene nanoribbons

Graphene nanoribbons are strips of graphene with narrow width ($\lesssim 50$ nm). If parallel edges are terminated with zigzag shape, it is called zigzag graphene nanoribbon. Tight-binding calculation predicts zigzag graphene nanoribbons to be metallic, however, density functional theory (DFT) calculations show that they are semiconducting, where the gap opens due to the antiferromagnetic spin coupling between carbon atoms on opposite edges. By employing Hubbard model, we can treat the interaction between electrons on a lattice site in addition to the hopping (or tunneling) of electrons between different sites of the lattice. Hubbard model takes the form

$$\hat{H} = t \sum_{\langle i, j \rangle, \sigma} \left(\hat{c}_{i\sigma}^{\dagger} \hat{c}_{j\sigma} + \hat{c}_{j\sigma}^{\dagger} \hat{c}_{i\sigma} \right) + U \sum_{i=1}^N \hat{n}_{i\uparrow} \hat{n}_{i\downarrow}, \quad (2.33)$$

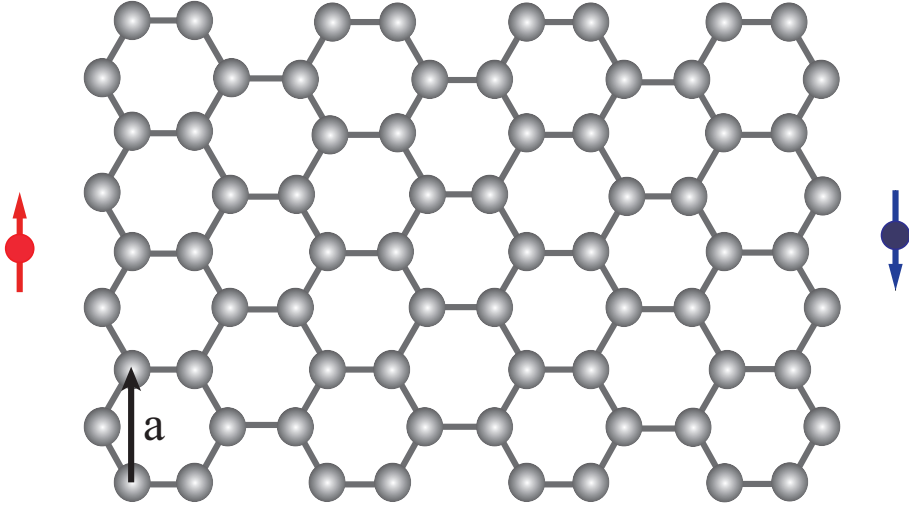


Figure 2.2: Zigzag graphene nanoribbon. \mathbf{a} denotes a lattice vector along which the system has 1D translational symmetry. Up and down arrows with circle at both edges are drawn to emphasize spin-polarized edge states.

where σ denotes spin degrees of freedom, U denotes repulsive interaction between electrons, and $\hat{n}_{i\sigma}$ denotes a number operator for an electron on i -th lattice site with spin σ . The first term is the usual tight-binding Hamiltonian and the second term indicates the on-site repulsive interaction between two electrons with opposite spins, which is a good approximation when the long-range part of Coulomb interaction is well screened and only short-range interaction becomes relevant. The existence of repulsion term in the Hubbard model Hamiltonian prevents the system becoming conducting, so it can be considered as an improvement on the tight-binding model for describing the metal-insulator transition. When U is finite, gap opens due to the an-

tiferromagnetic coupling between localized states at opposite edges as lowering the total energy, where the gap size is proportional to the magnitude of U . Carbon atoms on edges are considered to be passivated with a hydrogen atom. Within the mean field approximation (2.33) is simplified as

$$\hat{H} = \hat{H}_0 + U \sum_{i=1}^N (\hat{n}_{i\uparrow} \langle \hat{n}_{i\downarrow} \rangle + \langle \hat{n}_{i\uparrow} \rangle \hat{n}_{i\downarrow} - \langle \hat{n}_{i\uparrow} \rangle \langle \hat{n}_{i\downarrow} \rangle), \quad (2.34)$$

where

$$\hat{H}_0 = t \sum_{\langle i,j \rangle, \sigma} (\hat{c}_{i\sigma}^\dagger \hat{c}_{j\sigma} + \hat{c}_{j\sigma}^\dagger \hat{c}_{i\sigma}). \quad (2.35)$$

In this process, the two-particle interaction has been replaced by an interaction between a single particle and an effective field. Here, $\langle \hat{n}_{i\sigma} \rangle$ denotes the averaged occupation number of electrons with spin σ over all k points in the first Brillouin zone. Since the Hamiltonian depends on the electron number density, the equation should be solved self-consistently until the difference between input and output electron densities converges within a chosen criterion. In this way, we can get the appropriate energy band dispersions for semiconducting zigzag nanoribbons.

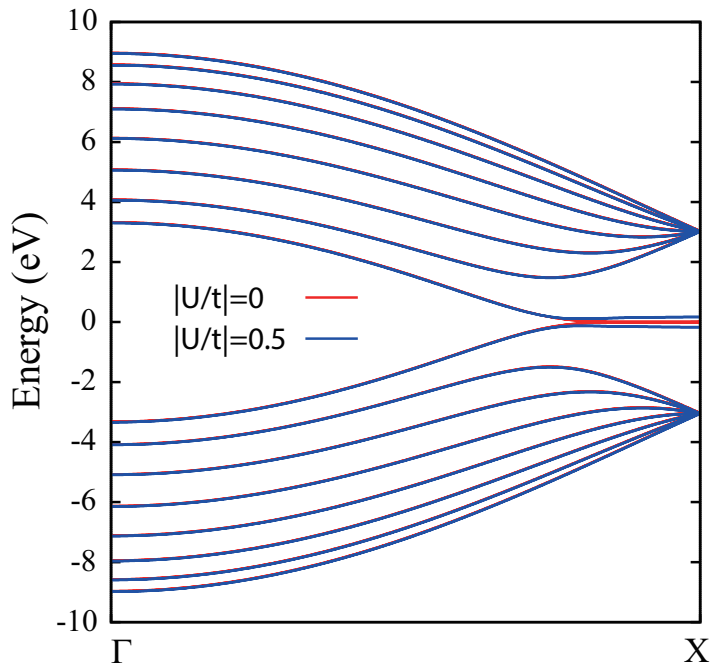


Figure 2.3: Tight-binding band structures of 8 zigzag graphene nanoribbon with and without on-site repulsion term. For finite U , band gap opens.

Chapter 3

Computational methods

3.1 Density functional theory

All the properties of a non-relativistic quantum system can be derived from the quantum mechanical wave function by solving the Schrödinger equation. In practice, however, solving the many-body problem within the wave function-based method is intractable in most cases. Modern density functional theory (DFT) has been one of the most successful method in condensed matter physics and quantum chemistry for calculating all the properties of quantum systems since its birth in 1964 [15]. The idea is to express the ground state energy of a many-body system in terms of electronic density as a fundamental variable. In this section, we briefly review DFT by introducing Hohenberg-Kohn theorem and Kohn-Sham formulation. After that, we examine local and semi-local approximations for exchange-correlation functional.

3.1.1 Hohenberg-Kohn theorem

Hohenberg-Kohn theorem establishes the solid mathematical basis of DFT, which consists of following two theorems.

Theorem 1. For any system of interacting particles in an external potential $V_{ext}(\mathbf{r})$, the potential $V_{ext}(\mathbf{r})$ is determined uniquely, up to addition by a constant, by the ground state particle density $n_0(\mathbf{r})$.

Proof Suppose that there were two external potentials $V_{ext,1}(\mathbf{r})$ and $V_{ext,2}(\mathbf{r})$ which differ by more than a constant and lead to the same ground state density $n(\mathbf{r})$. Corresponding two Hamiltonians, say H_1 and H_2 , have different ground state wave functions Ψ_1 and Ψ_2 , which are assumed to have the same ground state density $n_0(\mathbf{r})$. Since Ψ_2 is not the ground state of H_1 , it follows that

$$E_1 = \langle \Psi_1 | H_1 | \Psi_1 \rangle < \langle \Psi_2 | H_1 | \Psi_2 \rangle. \quad (3.1)$$

The strict inequality follows if the ground state is non-degenerate, yet the proof can readily be extended to degenerate cases [16]. The term in (3.1) can be written as

$$\langle \Psi_2 | H_1 | \Psi_2 \rangle = \langle \Psi_2 | H_2 | \Psi_2 \rangle + \langle \Psi_2 | H_1 - H_2 | \Psi_2 \rangle \quad (3.2)$$

$$= E_2 + \int d\mathbf{r} [V_{ext,1}(\mathbf{r}) - V_{ext,2}(\mathbf{r})] n_0(\mathbf{r}), \quad (3.3)$$

so that

$$E_1 < E_2 + \int d\mathbf{r}[V_{ext,1}(\mathbf{r}) - V_{ext,2}(\mathbf{r})]n_0(\mathbf{r}). \quad (3.4)$$

On the other hand if we consider E_2 in exactly the same way, we find the same expression only with the subscript 1 and 2 interchanged,

$$E_2 < E_1 + \int d\mathbf{r}[V_{ext,2}(\mathbf{r}) - V_{ext,1}(\mathbf{r})]n_0(\mathbf{r}). \quad (3.5)$$

Now if we combine (3.4) and (3.5), we arrive at the contradictory inequality $E_1 + E_2 < E_1 + E_2$. This inequality states that there cannot be two external potentials differing by more than a constant which give rise to the same non-degenerate ground state charge density. Thus, this proves the theorem. Since the Hamiltonian is uniquely determined except for a constant shift, the many-body wave functions for all states are obtained by solving the Schrödinger equation. Therefore all properties of the system are completely determined, provided the ground state density $n_0(\mathbf{r})$ is given.

Theorem 2. A universal functional for the energy $E[n]$ in terms of the density $n(\mathbf{r})$ can be defined, which is independent of the external potential $V_{ext}(\mathbf{r})$. For any particular $V_{ext}(\mathbf{r})$, the exact ground state energy of the system is the global minimum value of this functional, and the density $n(\mathbf{r})$ minimizing the functional is the exact ground

state density $n_0(\mathbf{r})$.

Proof Since all properties are uniquely determined if $n(\mathbf{r})$ is specified, each property can be viewed as a functional of $n(\mathbf{r})$ including the total energy functional

$$E_{HK}[n] = T[n] + E_{int}[n] + \int d\mathbf{r} V_{ext}(\mathbf{r})n(\mathbf{r}) + E_{II} \quad (3.6)$$

$$\equiv F_{HK}[n] + \int d\mathbf{r} V_{ext}(\mathbf{r})n(\mathbf{r}) + E_{II}, \quad (3.7)$$

where E_{II} is the interaction energy of the nuclei. The functional $F_{HK}[n]$ defined in (3.7) includes all internal energies, kinetic and potential, of the interacting electron system.

$$F_{HK}[n] = T[n] + E_{int}[n], \quad (3.8)$$

which depends only on the electron density and must be universal by construction.

Now consider a system with the ground state density $n_0(\mathbf{r})$ corresponding to an external potential $V_{ext}(\mathbf{r})$. Following the above discussion, the Hohenberg-Kohn functional is equal to the expectation value of the Hamiltonian in the unique ground state, which has wave function Ψ_0 , and

$$E_0 = E_{HK}[n_0] = \langle \Psi_0 | H_0 | \Psi_0 \rangle. \quad (3.9)$$

Now consider a different density $n(\mathbf{r})$, which undoubtedly corresponds to a different wave function Ψ . It follows that the energy E of this state is greater than E_0 , which can readily be shown since

$$E_0 = \langle \Psi_0 | H_0 | \Psi_0 \rangle < \langle \Psi | H_0 | \Psi \rangle = E. \quad (3.10)$$

Thus, the energy given by (3.10) in terms of the Hohenberg-Kohn functional evaluated for the correct ground state density $n_0(\mathbf{r})$ is indeed lower than the value evaluated for any other density $n(\mathbf{r})$. It follows that if the functional $F_{HK}[n]$ was known, by minimizing the total energy of the system with respect to variations in the density function $n(\mathbf{r})$, one would find the exact ground state density and ground state energy.

3.1.2 Kohn-Sham formulation

Hohenberg-Kohn theorem guarantees the existence of the energy functional, which, in principle, determines all the information of a many-body system. However, the theorem provides no practical guidance for constructing the functional. DFT has gained widespread interests only after Kohn and Sham had made the ansatz [17], which replaces the interacting many-body problem by an auxiliary independent-particle problem that can be solved more easily.

Now consider the Hohenberg-Kohn theorem, where the ground

state energy of a many-body system can be obtained by minimizing the energy functional (3.7) subjected to the constraint that the number of electrons N is conserved. The variational principle states that

$$\delta \left[F_{HK}[n] + \int d\mathbf{r} V_{ext}(\mathbf{r})n(\mathbf{r}) + E_{II} - \mu \left(\int d\mathbf{r}n(\mathbf{r}) - N \right) \right] = 0, \quad (3.11)$$

which leads to Euler-Lagrange's equation

$$\mu = \frac{\delta F_{HK}[n]}{\delta n(\mathbf{r})} + V_{ext}(\mathbf{r}), \quad (3.12)$$

where μ is the chemical potential. The earlier effort of Thomas and Fermi to express kinetic energy local in density has limitation since it is unable to hold bound states. Kohn and Sham's idea is that if one can find a system of non-interacting electrons that produces the same electronic density of the interacting system, the kinetic energy of the non-interacting system can be calculated exactly. This corresponds to express the many-body wave function as a single Slater determinant made of one-electron orbitals.

In the Kohn-Sham formulation the universal energy functional is divided into three terms; non-interacting kinetic energy T_s , Hartree energy (or classical Coulomb energy) $E_{Hartree}$, and exchange-correlation energy E_{xc} . The first two terms can be calculated exactly and compose

the majority of the total energy. All many-body effects of exchange and correlation are grouped into the third term. The expression for the kinetic energy is given by

$$T_s[n] = -\frac{\hbar^2}{2m} \sum_{i=1}^N \langle \psi_i | \nabla_i^2 | \psi_i \rangle, \quad (3.13)$$

and the Hartree energy is given by

$$E_{Hartree}[n] = \frac{1}{2} \int d\mathbf{r} \int d\mathbf{r}' \frac{n(\mathbf{r})n(\mathbf{r}')}{|\mathbf{r} - \mathbf{r}'|}. \quad (3.14)$$

Of course, non-interacting kinetic energy is not the exact kinetic energy of the interacting system and the missing fraction is due to the fact that the true many-body wave function cannot be written as a single Slater determinant. Deviation from the real kinetic energy must be included in the exchange-correlation energy term. Now the Euler-Lagrange's equation given in (3.12) becomes

$$\mu = \frac{\delta T_s[n]}{\delta n(\mathbf{r})} + V_{KS}(\mathbf{r}), \quad (3.15)$$

where $V_{KS}(\mathbf{r})$ is given by

$$V_{KS}(\mathbf{r}) = V_{ext}(\mathbf{r}) + V_{Hartree}(\mathbf{r}) + V_{xc}(\mathbf{r}), \quad (3.16)$$

with

$$V_{Hartree}(\mathbf{r}) = \int d\mathbf{r}' \frac{n(\mathbf{r}')}{|\mathbf{r} - \mathbf{r}'|}, \quad (3.17)$$

and

$$V_{xc}(\mathbf{r}) = \frac{\delta E_{xc}[n(\mathbf{r})]}{\delta n(\mathbf{r})}. \quad (3.18)$$

Expression (3.15) leads to the Kohn-Sham equation

$$\left[-\frac{\hbar^2}{2m} + V_{KS}(\mathbf{r}) \right] \psi_i(\mathbf{r}) = \varepsilon_i \psi_i(\mathbf{r}), \quad (3.19)$$

and the solutions of this one-body problem give the density of an auxiliary system

$$n(\mathbf{r}) = \sum_{i=1}^N |\psi_i(\mathbf{r})|^2, \quad (3.20)$$

which is obtained by filling the lowest N Kohn-Sham orbitals. It is worth mentioning that the density obtained by solving the Kohn-Sham equation for non-interacting electrons is the same as the exact ground state density. Therefore, if the exchange-correlation functional $E_{xc}[n(\mathbf{r})]$ defined in (3.18) were known, the exact ground state energy and density of the many-body system could be found by solving the Kohn-Sham equation for non-interacting electrons. Equation

(3.19) should be solved iteratively until the resulting electron density $n_{out}(\mathbf{r})$ coincides with the density $n_{in}(\mathbf{r})$ used for the construction of the Hamiltonian, which is solving Kohn-Sham equation in the self-consistent manner. Then the ground state energy is given by

$$E_{tot}[n] = \sum_{i=1}^N \epsilon_i - E_{Hartree}[n] + E_{xc}[n] - \int d\mathbf{r} \frac{\delta E_{xc}[n(\mathbf{r})]}{\delta n(\mathbf{r})} n(\mathbf{r}). \quad (3.21)$$

3.1.3 Approximations for exchange-correlation energy

The exact exchange-correlation functional $E_{xc}[n(\mathbf{r})]$, however, is unknown, hence the approximations made in the exchange-correlation functional limit the accuracy of the solutions of otherwise exact Kohn-Sham equation. In spite of the predictable complexity of the exact functional, great progress has been made with remarkably simple approximations. In this section two most widely used approximate functionals, local density approximation (LDA) and examples of generalized-gradient approximations (GGAs), are introduced.

In local density approximation it is assumed that the exchange-correlation energy functional depends solely on the value of the electronic density at each point in space. In other words, a general inhomogeneous electronic system is considered as "locally homogeneous" and the exchange-correlation energy is expressed as follows

assuming $\epsilon_{xc}[n] = \epsilon_{xc}(n(\mathbf{r}))$:

$$E_{xc}^{LDA}[n] = \int d\mathbf{r} n(\mathbf{r}) \epsilon_{xc}^{LDA}(n(\mathbf{r})). \quad (3.22)$$

where $\epsilon_{xc}^{LDA}(n(\mathbf{r}))$ is the exchange-correlation energy per electron of a homogeneous electron gas of density $n(\mathbf{r})$ and can be decomposed into exchange and correlation contributions

$$\epsilon_{xc}^{LDA}(n(\mathbf{r})) = \epsilon_x^{LDA}(n(\mathbf{r})) + \epsilon_c^{LDA}(n(\mathbf{r})). \quad (3.23)$$

It is natural, as well as successful, to start from the homogeneous electron gas (HEG) model where the ground state properties are determined by a constant electronic density. The exchange energy density takes on a simple analytic form for the HEG, which is given by Dirac's expression:

$$\epsilon_x^{LDA}(n(\mathbf{r})) = -\frac{3}{4} \left(\frac{3}{\pi} \right)^{1/3} n^{1/3} = -\frac{3}{4} \left(\frac{9}{4\pi^2} \right)^{1/3} \frac{1}{r_s}, \quad (3.24)$$

where $r_s = (3/4\pi n)^{1/3}$ is the average interelectronic distance in atomic unit (a_B). The unitless parameter r_s providing a measure of the electron density also represents the ratio of the average potential energy to the average kinetic energy of the system. Among diverse approximations for the correlation energy density, the most accurate result is parameterized by Perdew and Zunger based on the quantum Monte

Carlo simulations of Ceperley and Alder for the HEG [18].

$$\epsilon_c^{LDA,PZ}(n(\mathbf{r})) = \begin{cases} A n r_s + B + C r_s \ln r_s + D r_s, & \text{if } r_s \leq 1, \\ \gamma / (1 + \beta_1 \sqrt{r_s} + \beta_2 r_s), & \text{if } r_s > 1, \end{cases} \quad (3.25)$$

where coefficients are given by $A = 0.0311$, $B = -0.048$, $C = 0.002$, $D = -0.0116$, $\gamma = -0.1423$, $\beta_1 = 1.0529$, and $\beta_2 = 0.3334$ in Hartree units. Now, the exchange-correlation energy can be obtained by integrating the energy density value calculated with $n(\mathbf{r})$ in some neighborhood of point \mathbf{r} weighted with electronic density of the system.

Although far from being homogeneous, the surprising success of LDA in real systems comes from the presence of an exchange-correlation hole, which is defined as

$$n_{xc}(\mathbf{r}, \mathbf{r}') = n(\mathbf{r}') [g(\mathbf{r}, \mathbf{r}') - 1], \quad (3.26)$$

where pair correlation function $g(\mathbf{r}, \mathbf{r}')$ should be understood as averaged over the interaction strength in the spirit of adiabatic connection between non-interacting and fully interacting many-body system. Exchange-correlation hole represents a fictitious charge depletion due to the fact that the presence of an electron at \mathbf{r} reduces the probability of finding a second electron at \mathbf{r}' in the vicinity of \mathbf{r} , which is called exchange and correlation effect. Thus, it compen-

sates Hartree contribution which ignores this depletion. Another important property of exchange-correlation hole is that it satisfies the sum rule expressing the exchange-correlation hole contains exactly one displaced electron:

$$\int d\mathbf{r}' n_{xc}(\mathbf{r}, \mathbf{r}') = -1. \quad (3.27)$$

Given the exchange-correlation hole, the exchange-correlation energy density can be written as

$$\epsilon_{xc}(n(\mathbf{r})) = \frac{1}{2} \int d\mathbf{r}' \frac{n_{xc}(\mathbf{r}, \mathbf{r}')}{|\mathbf{r} - \mathbf{r}'|}. \quad (3.28)$$

The extension of the LDA to spin-polarized system is the local spin density approximation (LSDA), which is basically replacing the exchange-correlation energy density with a spin-polarized expression:

$$E_{xc}^{LSDA}[n_{\uparrow}(\mathbf{r}) + n_{\downarrow}(\mathbf{r})] = \int d\mathbf{r} [n_{\uparrow}(\mathbf{r}) + n_{\downarrow}(\mathbf{r})] \epsilon_{xc}^{hom}[n_{\uparrow}(\mathbf{r}) + n_{\downarrow}(\mathbf{r})] \quad (3.29)$$

$$= \int d\mathbf{r} n(\mathbf{r}) \epsilon_{xc}^{hom}[n(\mathbf{r}), \zeta], \quad (3.30)$$

where $\epsilon_{xc}^{hom}[n(\mathbf{r}), \zeta]$ is obtained by interpolation between the fully-polarized (ϵ_{xc}^P) and unpolarized (ϵ_{xc}^U) exchange-correlation energy den-

sities for HEG with some interpolating function $f(\zeta)$ depending on the magnetization density $\zeta = n_{\uparrow}(\mathbf{r}) - n_{\downarrow}(\mathbf{r})$:

$$\epsilon_{xc}^{hom}[n(\mathbf{r}), \zeta] = f(\zeta)\epsilon_{xc}^P[n(\mathbf{r})] + [1 - f(\zeta)]\epsilon_{xc}^U[n(\mathbf{r})]. \quad (3.31)$$

Encouraged by the success of LSDA, various efforts have been made to address the inhomogeneities in the electronic density. That is to carry out an expansion of the density in terms of the gradient and higher order derivatives. This idea led to gradient expansion approximation (GEA), where the general expression for the exchange-correlation energy can be written in the following form:

$$E_{xc}[n] = \int d\mathbf{r} n(\mathbf{r}) \epsilon_{xc}[n(\mathbf{r})] F_{xc}[n(\mathbf{r}), \nabla n(\mathbf{r}), \nabla^2 n(\mathbf{r}), \dots], \quad (3.32)$$

where the function F_{xc} is an enhancement factor modifying the LDA expression. However, GEA does not lead to the desired accuracy, but frequently worsens the LDA results due to the violation of the conditions required for the exchange-correlation hole, such as a sum rule, long-range decay, etc. The name generalized gradient approximation (GGA) has been given to various modified GEAs that preserve the desired properties of exchange-correlation hole. Among various GGA functionals, the most popular one is proposed by Perdew, Burke, and Ernzerhof (PBE) [19]. The chosen expression for the enhancement

factor for exchange part defined in (3.32) is

$$F_x(s) = 1 + \kappa - \frac{\kappa}{1 + \mu s^2 / \kappa}, \quad (3.33)$$

where $\mu = 0.21951$, $\kappa = 0.804$, and the dimensionless density gradient $s = |\nabla n| / (2k_F n)$. The correlation energy assumes the form

$$E_c^{GGA}[n] = \int d\mathbf{r} n(\mathbf{r}) \left[\epsilon_c^{hom}(n, \zeta) + H(n, \zeta, t) \right], \quad (3.34)$$

where $\epsilon_c^{hom}(n, \zeta)$ is the correlation energy density for HEG defined in (3.31). Here, the correlation correction term H is

$$H(n, \zeta, t) = \frac{e^2}{a_0} \gamma \phi^3 \ln \left[1 + \frac{\beta}{\gamma} t^2 \left(\frac{1 + At^2}{1 + At^2 + A^2 t^4} \right) \right], \quad (3.35)$$

with

$$A = \frac{\beta}{\gamma} \left[\exp \left(\frac{-\epsilon_c^{hom}(n)}{\gamma \phi^3 e^2 / a_0} \right) - 1 \right]^{-1}, \quad (3.36)$$

where $\beta = 0.066725$, $\gamma = 0.031091$, and $t = |\nabla n| / (2\phi k_s n)$ is a dimensionless density gradient with $k_s = \sqrt{4k_F / \pi a_0}$ is the Thomas-Fermi screening wave number. Here $\phi(\zeta) = [(1 + \zeta)^{2/3} + (1 - \zeta)^{2/3}] / 2$ is a spin-scaling factor.

3.2 Pseudopotential plane wave approach

3.2.1 Plane wave basis set

Solving the electronic structure problem in practice requires a choice of mathematical representation for the one-electron wave functions, which can be expanded as a linear combination of a generic basis set $|\phi_\alpha\rangle$. In real-space representation, the one-electron wave function is written as

$$\psi_i(\mathbf{r}) = \sum_{\alpha=1}^M c_{i\alpha} \phi_\alpha(\mathbf{r}), \quad (3.37)$$

where the sum runs over all the basis functions up to the size of the basis set M , which determines the accuracy of the calculation. For a periodic system, Bloch's theorem states that the eigenstates of the one-electron Hamiltonian can be written as a plane wave times a periodic function with the periodicity of the lattice, i.e., $u_{\mathbf{k}}(\mathbf{r}) = u_{\mathbf{k}}(\mathbf{r} + \mathbf{R})$ with \mathbf{R} is any lattice vector. Plane waves (PWs) are solutions of the Schrödinger equation in the presence of a constant external potential, which are approximate solutions in interstitial regions in condensed phases. Closer to nuclei, however, the external potential is far from constant, so the solutions of Schrödinger equation have to be written as linear combinations of PWs. In general, any function in real space can be written as a Fourier transformation of a function in reciprocal

space,

$$u_{\mathbf{k}}(\mathbf{r}) = \int d\mathbf{g} e^{i\mathbf{g}\cdot\mathbf{r}} \tilde{u}_{\mathbf{k}}(\mathbf{g}). \quad (3.38)$$

The periodicity of $u_{\mathbf{k}}(\mathbf{r})$ allows only the values of \mathbf{g} satisfying the relation $e^{i\mathbf{g}\cdot\mathbf{a}_j} = 1$, that is $\mathbf{g}\cdot\mathbf{a}_j = 2n\pi$ for primitive lattice vectors \mathbf{a}_j , where $j = 1, 2, 3$ and n is integer number. This implies that $\mathbf{g} = n_1\mathbf{b}_1 + n_2\mathbf{b}_2 + n_3\mathbf{b}_3$ (n_i : integer numbers), where

$$\mathbf{b}_i = 2\pi \frac{\mathbf{a}_j \times \mathbf{a}_k}{\Omega_{cell}} \quad (3.39)$$

with $\Omega_{cell} = \mathbf{a}_1 \cdot (\mathbf{a}_2 \times \mathbf{a}_3)$ is the primitive unit cell volume. Therefore, the \mathbf{g} vectors in (3.38) are precisely restricted to the reciprocal lattice vectors \mathbf{G} , and the general expression for the Bloch function is

$$\psi_{\mathbf{k}}(\mathbf{r}) = \frac{e^{i\mathbf{k}\cdot\mathbf{r}}}{\sqrt{\Omega}} \sum_{\mathbf{G}=0}^{\infty} c_{\mathbf{k}}(\mathbf{G}) e^{i\mathbf{G}\cdot\mathbf{r}}, \quad (3.40)$$

where the Fourier coefficients are $c_{\mathbf{k}}(\mathbf{G})$. This restriction of the possible values of \mathbf{g} to the reciprocal lattice vectors ensures that periodicity of the crystal is automatically verified, and the Fourier transform (3.38) becomes the Fourier series (3.40). We now define the PW basis

functions

$$\phi_{\mathbf{G}}(\mathbf{r}) = \frac{1}{\sqrt{\Omega}} e^{i\mathbf{G}\cdot\mathbf{r}} \quad (3.41)$$

which are normalized over the volume $\Omega = N_{cell}\Omega_{cell}$

$$\langle \phi_{\mathbf{G}} | \phi_{\mathbf{G}'} \rangle = \frac{1}{\Omega} \int_{\Omega} d\mathbf{r} e^{i(\mathbf{G}-\mathbf{G}')\cdot\mathbf{r}} = \frac{1}{\Omega} (\Omega \delta_{\mathbf{G},\mathbf{G}'}) = \delta_{\mathbf{G},\mathbf{G}'}, \quad (3.42)$$

so that PWs corresponding to different wave vectors, $\mathbf{G} \neq \mathbf{G}'$, are orthonormal. With this definition, the wave functions for the different eigenstates i can be written as

$$\psi_{i\mathbf{k}}(\mathbf{r}) = e^{i\mathbf{k}\cdot\mathbf{r}} \sum_{\mathbf{G}=0}^{\infty} c_{i\mathbf{k}}(\mathbf{G}) \phi_{\mathbf{G}}(\mathbf{r}). \quad (3.43)$$

Notice that the phase factor $e^{i\mathbf{k}\cdot\mathbf{r}}$ involves a wave vector \mathbf{k} in the first Brillouin zone (BZ), while the reciprocal lattice vectors \mathbf{G} entering the PW expansion, except for $\mathbf{G} = 0$, lie always outside the BZ. Wave functions corresponding to different \mathbf{k} vectors obey separate Schrödinger equations.

In principle, an infinite number of \mathbf{G} vectors are required to represent the wave functions with infinite accuracy. In practice, however, the Fourier coefficients $c_{\mathbf{k}}(\mathbf{G})$ of the wave functions decrease with increasing $|\mathbf{k} + \mathbf{G}|$, so the PW expansion can be effectively truncated at

a finite number of terms, i.e. limited to all waves of which kinetic energy is lower than a certain energy cutoff E_{cut} :

$$\frac{\hbar^2}{2m} |\mathbf{k} + \mathbf{G}|^2 < E_{cut}. \quad (3.44)$$

For the Γ -point ($\mathbf{k} = 0$), the above expression defines a sphere of radius G_{cut} in the space of wave vectors, which is given by

$$|\mathbf{G}| < G_{cut} = \sqrt{\frac{2mE_{cut}}{\hbar^2}}. \quad (3.45)$$

The truncation of the basis set leads to errors in the computed physical quantities, but these errors can be easily handled by increasing the cutoff. Since this implies an increase in the size of the basis set without modifying the Hamiltonian, the energy should decrease variationally with increasing E_{cut} . This systematic enhancement of accuracy with the increase of basis set size differentiates PW basis functions from other non-orthogonal (e.g. Gaussians) basis functions.

3.2.2 Pseudopotential theory

The strong atomic Coulomb potential leads to wave functions rapidly varying, sometimes involving sharp peaks, in the vicinity of nuclei, which can hardly be expanded in finite PW basis functions. The fundamental idea of pseudopotential [20] is to replace the strong Coulomb

potential of the nucleus and the tightly bound core electrons by an effective ionic potential, or screened potential acting on the valence electrons. We start with defining the core electrons and the valence electrons. Electronic states of an atom can be classified into core states, which are highly localized and not involved in chemical bondings, and valence states, which are extended and responsible for chemical bondings. Based on the observations that core states are not essential for the description of chemical bondings, and a good description of the valence wave functions inside the core region is not strictly necessary, there is no lack of crucial information if the inner solution (inside some cutoff radius) is replaced with a smooth, nodeless pseudo-wave function, which is not a solution to the original atomic problem. Now it is reasonable, in practice, to expand pseudo-wave functions with a truncated basis set.

The origin of the modern pseudopotential approach can be traced back to the famous paper of Philips and Kleinman [21], which showed that one can construct a smooth valence wave function $\tilde{\psi}_v$ that is not orthogonalized to the core states ψ_c , by combining the core and the true valence wave function ψ_v in the following way:

$$|\tilde{\psi}_v\rangle = |\psi_v\rangle + \sum_c \alpha_{cv} |\psi_c\rangle, \quad (3.46)$$

where $\alpha_{cv} = \langle \psi_c | \tilde{\psi}_v \rangle \neq 0$. This pseudo-wave function satisfies the

modified Schrödinger equation:

$$\left[\hat{H} + \sum_c (\epsilon_v - \epsilon_c) |\psi_c\rangle\langle\psi_c| \right] |\tilde{\psi}_v\rangle = \epsilon_v |\tilde{\psi}_v\rangle. \quad (3.47)$$

Here, $\hat{H} = \hat{T} + \hat{V}$, where $\hat{V} = (Z_c/r)\hat{I}$ is the bare nuclear potential and \hat{I} is the identity operator. This shows that it is possible to construct a pseudo-Hamiltonian

$$\hat{H}_{PS} = \hat{H} + \sum_c (\epsilon_v - \epsilon_c) |\psi_c\rangle\langle\psi_c|, \quad (3.48)$$

with the same eigenvalues of the original Hamiltonian but with the smoother and nodeless wave functions. The associated potential

$$\hat{V}_{PS} = \frac{Z_c}{r}\hat{I} + \sum_c (\epsilon_v - \epsilon_c) |\psi_c\rangle\langle\psi_c| \quad (3.49)$$

was named *pseudopotential*. This pseudopotential acts differently on wave functions of different angular momentum, and the most general form of such a pseudopotential takes following form:

$$\hat{V}_{PS}(\mathbf{r}) = \sum_{l=0}^{\infty} \sum_{m=-l}^l v_{PS}^l(r) |lm\rangle\langle lm| = \sum_{l=0}^{\infty} v_{PS}^l(r) \hat{P}_l, \quad (3.50)$$

where $\langle \mathbf{r} | lm \rangle = Y_{lm}(\theta, \phi)$ are spherical harmonics, $v_{PS}^l(r)$ is the pseudopotential corresponding to the angular component l , and the oper-

ator

$$\hat{P}_l = \sum_{m=-l}^l |lm\rangle\langle lm| \quad (3.51)$$

is a projection operator onto the l -th angular momentum subspace. Pseudopotential of this kind is usually called *semi-local* (or angular-dependent) pseudopotential because it acts differently on the various angular momentum components of the wave function. It is because of the different orthogonality conditions for states with different l components. Also, for each angular momentum l the pseudopotential have the valence l -state as the ground state.

Normally, only a few (up to l_{max}) low-angular-momentum core states are occupied. Therefore, for values of $l > l_{max}$ the ionic core is seen in the same way by all the l components of the wave functions, and the summation in (3.50) can be rewritten as

$$\hat{V}_{PS}(\mathbf{r}) = \sum_{l=0}^{\infty} v_{PS}^{loc}(r) \hat{P}_l + \sum_{l=0}^{l_{max}} \left[v_{PS}^l(r) - v_{PS}^{loc}(r) \right] \hat{P}_l \quad (3.52)$$

$$= V^{loc}(r) + \sum_{l=0}^{l_{max}} \Delta v_{PS}^l(r) \hat{P}_l. \quad (3.53)$$

Here, $\Delta v_{PS}^l(r)$ are short-ranged functions confined to the core region, and $V^{loc}(r)$ is an average local potential that represents the screened Coulomb interaction and is required to represent the potential that

acts on higher angular momentum components.

In actual calculation, if we assume the semi-local form defined in (3.53), the matrix elements of the pseudopotential can be obtained by double integral over variables. While angular-dependent parts can be integrated separately (non-local in l and m), a radial integral cannot be separated due to a factor $\delta(r - r')$ implied in the form (local in r), which is generally too costly. Thus, for a large number of PW basis functions, this radial integration indeed becomes a bottleneck for electronic structure calculation with many atoms. It is known that this problem does not arise in fully non-local pseudopotentials such as the original Philips-Kleinman form (3.49). From this observation, Kleinman and Bylander developed a fully non-local (non-local in l, m , and r) separable form of the pseudopotential [22], which can replace the semi-local part in (3.53) to a good approximation. The total pseudopotential now takes the form

$$\hat{V}_{KB} = V^{local}(r) + \sum_{lm} \frac{|\Delta\hat{v}_{PS}^l \Psi_{PS}^{lm}\rangle \langle \Psi_{PS}^{lm} \Delta\hat{v}_{PS}^l|}{\langle \Psi_{PS}^{lm} | \Delta\hat{v}_{PS}^l | \Psi_{PS}^{lm}\rangle}. \quad (3.54)$$

This operator acts on a reference state $|\Psi_{PS}^{lm}\rangle$ in an identical manner to the original semi-local operator \hat{V}_{PS} .

The construction of a pseudopotential, however, is not unique problem, which allows the freedom to choose forms that simplify the calculations and the interpretation of the resulting electronic struc-

ture. It is essential to know that all properties of the wave function outside the scattering region are invariant to a change in the phase shift by any multiple of 2π . This requires that the pseudopotential should be constructed in such a way that its scattering properties (or phase shifts) are the same as those of the all-electron potential, although the radial pseudo-wave function has no nodes inside the core region. The desired property of a pseudopotential is that it should be transferable as well as soft. Transferability means that a pseudopotential constructed in one environment (usually the atom) can faithfully represent the valence properties (scattering properties) in different environments including ions, molecules, and condensed matter, where the eigenvalues shift from their atomic values. Hamann, Schulüter, and Chiang (HSC) found that transferability is ensured by imposing *norm-conservation* condition:

$$\int_0^{r_c} dr r^2 [R_{PS}^l(\epsilon, r)]^2 = \int_0^{r_c} dr r^2 [R_{AE}^l(\epsilon, r)]^2. \quad (3.55)$$

A key result of HSC was to realize that the norm of the wave function also appears in a very important identity to the Friedel sum rule:

$$-\frac{1}{2} \left\{ [rR^l(\epsilon, r)]^2 \frac{d}{d\epsilon} \frac{d}{dr} \ln R^l(\epsilon, r) \right\}_{r_c} = \int_0^{r_c} dr r^2 [R^l(\epsilon, r)]^2. \quad (3.56)$$

Therefore, the norm-conservation condition imposes that, to first-order

in the eigenvalue, the logarithmic derivatives of the all-electron and pseudo-wave functions vary in the same way. This implies that a small change in the eigenvalue due to changes in the external potential (the environment) produces only a second-order change in the logarithmic derivative. In this way, pseudopotentials derived from atomic calculations can be exported to other environments.

The norm-conservation constraint is tightly linked to the concept of transferability through the sum rule defined in (3.35), which is responsible for the requirement of the high PW cutoff of some pseudopotentials, e.g. O $2p$ or Cu $3d$. However, it is not strictly necessary that the norms of the all-electron and pseudo-wave functions coincide. In 1990 Vanderbilt has relaxed the norm-conservation condition by generalizing the sum rule, who showed that much smoother, but still highly transferable, pseudopotentials can be obtained. These have received the name of *ultrasoft* (US) pseudopotentials. In US, the sum rule is modified to

$$-\frac{1}{2} \left\{ [rR^l(\epsilon, r)]^2 \frac{d}{d\epsilon} \frac{d}{dr} \ln R^l(\epsilon, r) \right\}_{r_c} = \langle \Psi_{PS}^{ilm} | \Psi_{PS}^{ilm} \rangle_{r_c} + Q_{ii}^l. \quad (3.57)$$

The matrix elements Q_{ii}^l represents the amount of charge missing in the pseudo-wave function of angular momentum l , calculated using the reference energy ϵ_{il} .

3.2.3 Projector augmented method

Although pseudopotential reduces the number of wave functions to be calculated and removes the singular behavior of ionic potential at the lattice point, the information on the full wave function close to the nuclei is lost in the approach. A different approach is the augmented plane wave method (APW), where space is divided into atom-centered augmentation spheres, inside which the wave functions are taken as some atom-like partial waves, and bonding regions outside the spheres, in which some envelope functions are defined. The partial waves and envelope functions are then matched at the boundaries of the spheres. A more general approach is the projector augmented wave method (PAW), which was first proposed by Blöchl [23]. This approach retains the all-electron character, but it uses a decomposition of the all-electron wave function in terms of a smooth pseudo-wave function, and a rapidly varying contribution localized within the core region. The true and pseudo-wave functions are related by a linear transformation [24]:

$$\mathcal{T} = \mathbf{1} + \sum_m (|\Psi_{AE}^m\rangle - |\Psi_{PS}^m\rangle)\langle\tilde{p}^m|, \quad (3.58)$$

where the indices m run over all projectors on all atoms. This transformation leads to

$$|\Psi_{AE}^n\rangle = \mathcal{T} |\Psi_{PS}^n\rangle = |\Psi_{PS}^n\rangle + \sum_m (|\Psi_{AE}^m\rangle - |\Psi_{PS}^m\rangle) \langle \tilde{p}^m | \Psi_{PS}^n \rangle \quad (3.59)$$

where $\Psi_{AE}^m(\mathbf{r})$ are all-electron partial waves obtained for a reference atom, $\Psi_{PS}^m(\mathbf{r})$ are pseudo-atomic partial waves that coincide with the all-electron one outside a cutoff radius and can be any smooth continuation inside, and $|\tilde{p}^m\rangle$ are projectors that verify the duality relation

$$\langle \tilde{p}^m | \Psi_{PS}^n \rangle = \delta_{mn}. \quad (3.60)$$

The PAW transformation provides a way to calculate all-electron observables using this smooth pseudo wave function from a pseudopotential calculation, conveniently avoiding having to ever represent the all-electron wavefunction explicitly in memory. Now we can define the *pseudo operator* for any operator \hat{A} in the all-electron problem by employing the transformation operator \mathcal{T} as

$$\hat{A} = \mathcal{T}^\dagger \hat{A} \mathcal{T} = \hat{A} + \sum_{mm'} |\tilde{p}^m\rangle \left\{ \langle \Psi_{AE}^m | \hat{A} | \Psi_{AE}^{m'} \rangle - \langle \Psi_{PS}^m | \hat{A} | \Psi_{PS}^{m'} \rangle \right\} \langle \tilde{p}^{m'} |. \quad (3.61)$$

The PAW method is typically combined with the frozen core approximation, in which the core states are assumed to be unaffected by the ion's environment. Therefore, every pseudopotential machinery is available for the PAW method, which just has to be supplemented with contributions from spherical regions.

3.3 Van der Waals interaction

The van der Waals (vdW) interaction can be illustrated as a non-directional interaction between non-overlapping electron densities with induced dipole moments, where instantaneous polarization arises from the charge fluctuation of quantum system. This vdW interaction is obviously the instantaneous correlation effect and cannot be correctly described by the approximated exchange-correlation functionals in DFT. One way to treat vdW interaction in DFT calculation is adding a semi-empirical dispersion potential to the Kohn-Sham energy. Then the total energy is given by

$$E_{DFT-D} = E_{KS-DFT} + E_{disp}, \quad (3.62)$$

where E_{KS-DFT} is the usual self-consistent Kohn-Sham energy as obtained from the chosen density functional and E_{disp} is empirical dis-

persion potential given by

$$E_{disp} = - \sum_{i,j} \sum_L \frac{C_6^{ij}}{R_{ij,L}^6} f_{d,s_6}(R_{ij,L}), \quad (3.63)$$

where the summations are over all atoms (i and j) and all repeated unit cells (L), C_6^{ij} denotes the dispersion coefficient for a pair of atoms, $R_{ij,L}$ is the interatomic distance between an atom in a reference cell centered at origin and another atom in the L-th cell, and $f(R_{ij,L})$ is a damping function to scale the force field such as to minimize contributions from interactions within typical bonding distances. Interactions over a certain suitably chosen cutoff radius give negligible contributions to E_{disp} and can be ignored safely. In the original method of Grimme, Fermi-type damping function is used [25]:

$$f_{d,s_6}(R_{ij}) = \frac{s_6}{1 + e^{-d(R_{ij}/(s_R R_{0ij}) - 1)}}, \quad (3.64)$$

where d is a damping parameter, R_{0ij} is the sum of atomic vdW radii of atom pair ij, s_R is a scaling factor, and s_6 is a global scaling factor that only depends on the density functional used and has been optimized for several different DFT functionals such as PBE ($s_6 = 0.75$), BLYP ($s_6 = 1.2$), and B3LYP ($s_6 = 1.05$). Parameters C_6^{ij} and R_{0ij} are

computed using the following combination rules:

$$C_6^{ij} = \sqrt{C_6^{ii}C_6^{jj}}, \quad (3.65)$$

which is a geometric mean of two atomic C_6 coefficients, and

$$R_{0ij} = R_{0i} + R_{0j}. \quad (3.66)$$

The values of C_6^{ii} and R_{0i} are tabulated for each element and are insensitive to the particular chemical situation (for instance, C_6 for carbon in methane takes exactly the same value as that for C in benzene within this approximation).

3.4 *Ab initio* force constant methods

The calculation of vibrational spectra is essential to investigate phase stability and thermodynamics of the crystalline materials. *Ab initio* approaches for a calculation of phonon dispersion relations are categorized into the linear response approach and the direct approach. Linear response approach denotes the method in which the dynamical matrix is expressed in terms of the inverse dielectric matrix describing the response of the valence electron density to a periodic lattice perturbation. This is difficult to be exploited for a number of systems because the dielectric matrix should be calculated by means of

the electronic eigenfunctions and eigenvalues of the perfect crystal. In a direct approach, the energy of a phonon is calculated as a function of the displacement amplitude in terms of the difference in the energies of the distorted and the unperturbed lattice, which is called the frozen phonon method. This approach is restricted to phonons whose wavelength is compatible with the supercell used in the calculation. Another variant of the direct approach is the force constant method. In the force constant method, the elements of the force-constant matrix are calculated from the forces obtained by the use of the Hellmann-Feynman theorem, or force theorem, in total energy calculation. Then the dynamical matrix is determined by a Fourier transformation, and the phonon frequencies for arbitrary wave vectors are evaluated by a diagonalization of this matrix. Among the forgoing *ab initio* approaches, we elaborate on the force constant method in this section [26, 27].

The *ab initio* force constant approach is based on the periodically repeated supercells. First consider that a single atom in such a supercell is displaced by $\mathbf{u}_{j\mathbf{v}}$ from its equilibrium position, where j is the index of the primitive unit cell and \mathbf{v} is atomic index. Because of the periodic boundary condition, the induced force acting on all other atoms in the supercell comes from the equivalently displaced atoms in the repeated images of the supercell as well as the displaced atom inside the supercell. Here we define the equilibrium position of

μ -th atom in i -th primitive unit cell as $\mathbf{R}_{i\mu} = \mathbf{R}_i + \mathbf{d}_\mu$, where \mathbf{R}_i is the lattice vector and \mathbf{d}_μ is the equilibrium position of the atom within the primitive unit cell. Under the harmonic approximation, the force acting on μ -th atom in i -th primitive unit cell is given by

$$\mathbf{F}(\mathbf{R}_{i\mu}, \mu) = - \sum_{\mathbf{L}} \mathbf{D}(\mathbf{R}_{i\mu}, \mu; \mathbf{R}_{j\nu} + \mathbf{L}, \nu) \cdot \mathbf{u}_{j\nu}, \quad (3.67)$$

where $\mathbf{D}(\mathbf{R}_{i\mu}, \mu; \mathbf{R}_{j\nu} + \mathbf{L}, \nu)$ are (3×3) harmonic force constant matrices relating atoms $(\mathbf{R}_{i\mu}, \mu)$ and $(\mathbf{R}_{j\nu} + \mathbf{L}, \nu)$, and \mathbf{L} are indices of supercell lattice vectors. When taking into account the summation over supercells \mathbf{L} , the cumulant force constant matrix is defined as

$$\mathbf{D}_\Sigma(\mathbf{R}_{i\mu}, \mu; \mathbf{R}_{j\nu}, \nu) = \sum_{\mathbf{L}} \mathbf{D}(\mathbf{R}_{i\mu}, \mu; \mathbf{R}_{j\nu} + \mathbf{L}, \nu) \quad (3.68)$$

The aim of the direct method is to describe the dynamical matrix $D(\mathbf{k})$ of the crystal, which is defined as

$$D(\mathbf{k}; \mu\nu) = \frac{1}{\sqrt{M_\mu M_\nu}} \sum_{\mathbf{L}} \sum_j \mathbf{D}(\mathbf{R}_{i\mu}, \mu; \mathbf{R}_{j\nu} + \mathbf{L}, \nu) \times \exp \{ -i\mathbf{k} \cdot [\mathbf{R}_{i\mu} - \mathbf{R}_{j\nu} - \mathbf{L}] \}. \quad (3.69)$$

Here the summation j runs over all primitive unit cells in a supercell, M_μ, M_ν and $\mathbf{R}_{i\mu}, \mathbf{R}_{j\nu}$ are masses and positions of atoms, respectively. Using the cumulant force constants defined in (3.73), one may define

an approximate dynamical matrix as

$$\tilde{D}(\mathbf{k}; \mu\nu) = \frac{1}{\sqrt{M_\mu M_\nu}} \sum_j \mathbf{D}_\Sigma(\mathbf{R}_{i\mu}, \mu; \mathbf{R}_{j\nu}, \nu) \times \exp\{-i\mathbf{k} \cdot [\mathbf{R}_{i\mu} - \mathbf{R}_{j\nu}]\}. \quad (3.70)$$

At the wave vector $\mathbf{k}_\mathbf{L}$ fulfilling the condition

$$\exp(i\mathbf{k}_\mathbf{L} \cdot \mathbf{L}) = 1, \quad (3.71)$$

which is usually the case of the high-symmetry \mathbf{k} points, the approximate and the exact dynamical matrices are equal, i.e., $D(\mathbf{k}; \mu\nu) = \tilde{D}(\mathbf{k}; \mu\nu)$. Nonetheless, increasing the size of the supercell, better accuracy of the phonon dispersion curves is achieved. The advantage of the introduced direct method is that it does not impose any limit to the range of interaction. The method interpolates the dispersion curves between exact points; however, if the force constants outside the supercell are so small that they could be neglected, then the dispersion curves are exact for all the wave vectors. Finally, the equation of motion for each value of \mathbf{k} and branch index s is written as

$$\sum_\nu \tilde{D}(\mathbf{k}; \mu\nu) \varepsilon_s(\nu; k) = M_\mu \omega_s(k)^2 \varepsilon_s(\mu; k), \quad (3.72)$$

where ε_s are polarization vectors satisfying the generalized orthogo-

nality relations

$$\sum_{\mu} M_{\mu} \varepsilon_{s'}(\mu; k)^* \varepsilon_s(\mu; k) = \delta_{ss'}. \quad (3.73)$$

Both ε_s and $\omega_s(k)$ are determined by the diagonalization of $\tilde{D}(\mathbf{k}; \mu\nu)$:

$$\sum_{\mu\nu} \varepsilon_{s'}(\mu; k)^* \tilde{D}(\mathbf{k}; \mu\nu) \varepsilon_s(\nu; k) = \omega(k)_s^2 \delta_{ss'}. \quad (3.74)$$

Chapter 4

Phonon softening and mechanical failure of graphene under tensile strain

Phonon softening of graphene under tensile strain is investigated based on *ab initio* density functional theory calculations. From calculated phonon band structures, we show that the Kohn anomaly point shifts from a high-symmetry k point to a lower symmetry one under the symmetry lowering tensile strain as a consequence of the Dirac point shift in the electronic band structure. We demonstrate that, over a wide range of tensile strain directions, the strain-induced enhancement of phonon softening can give rise to phonon instabilities resulting in a mechanical failure of graphene. It is shown that there are two types of instabilities associated with phonons near K and Γ points, respectively, which induce symmetry-breaking structural distortions, and both of them lead to mechanical failure prior to the elastic failure commonly expected when the structural symmetry is retained.

4.1 Introduction

The ultimate strength of a material, defined to be the maximum achievable stress that can be supported prior to material failure, is a crucial quantity that characterizes the mechanical property of a material. The ultimate strength under ideal conditions (i.e., homogeneous deformation in a defect-free structure) is closely related to the intrinsic atomic bond strength. Such an ideal strength of a material becomes an important issue with increasing interest in synthesizing almost perfect materials and searching for ultrastrength materials these days [28, 29].

The measurement of the ideal strength, however, has remained elusive for quite a long time because the actual breaking strength of a brittle material is governed by the existence of flaws within the material rather than the intrinsic strength of its atomic bonds [30]. Recently, progresses in graphene research have made possible [1, 4] the synthesis of large-area defect-free graphene and the direct measurement of its ideal strength. Especially, Lee et al. measured the mechanical properties of monolayer graphene membranes suspended over open holes by using an atomic force microscope (AFM) nano indentation, and the strength of graphene appears nearly ideal and exceeds, as predicted, the strength of any other materials [31]. This experiment inspires the question of how graphene fails under ideal conditions, and recent theories reveal that the failure mechanism of

graphene under equibiaxial strain lies in phonon instability associated with Kohn anomaly occurring at a critical strain of $\sim 15\%$ [32–34]. This is far below the critical strain for the elastic failure occurring at more than 20%. The elastic failure corresponds to the maximum stress before bond breaking under the constraint of maintaining the primitive unit cell of the graphene lattice [32]. For the uniaxial strain, however, it is known that there is no such kind of instability prior to elastic failure [33], which implies that applied strain configurations should affect not only the magnitude of the strength but also the failure mechanism in graphene. In practical situations, strain may be applied in general directions and the mechanical failure mechanism can be different depending on the direction of the strain. There was a Density Functional Theory (DFT) study which compared the strength of the $\sqrt{3} \times \sqrt{3}$ unit cell (K-cell) and that of the primitive cell under strain states of graphene to investigate a particular symmetry-lowering process [32], but K-cell cannot describe phonon instability under strain states other than biaxial strain. Therefore, we explore the conditions under which the phonon instability occurs prior to the elastic failure, and the process how phonon softening develops for given strain states. In this work, we find that there are two types of phonon instabilities associated with K- and Γ -phonons that precede the usual elastic failure for almost all strain states. We will explain how these instabilities are related to the symmetry and the electronic structure

of graphene by investigating the effects of general strain states on the phonon spectra based on the DFT calculations. In selected cases, we will further show that these phonon instabilities are indeed responsible for a structural phase transition and the resulting mechanical failure of graphene.

The failure of graphene under biaxial tensile strain is known to be triggered by the strain-induced enhancement of the Kohn anomaly [32, 33]. The Kohn anomaly in the phonon dispersion in metals is a discontinuity in its derivative with considerable phonon frequency softening at nesting vectors in the Fermi surface [35]. Occurrence of the Kohn anomaly in a metallic system depends on the Fermi surface geometry and the nature of the electron screening of the electric field produced by the ionic lattice. For graphene, the Kohn anomaly can be characterized by kinks in the highest optical branch at Γ and K (K'). The Kohn anomaly at Gamma (Γ) is originated from the intra-valley scattering at Dirac points, but it does not determine the graphene strength because the corresponding phonon mode has a much weaker electron-phonon coupling strength than the phonon mode at K [36]. The Kohn anomaly at K is caused by the point-like topology of the graphene Fermi surface, which allows for the Fermi surface nesting like a 1-D system with the nesting vector corresponding to \mathbf{K} . This Fermi surface nesting vector enables the inter-valley scattering from K to K' , and under intense strain this anomaly can lead to the so-

called Kekule distortion [34], where the lattice consists of alternating short and long bonds between neighboring carbon atoms [37]. Such a distortion is realized under large applied strain by exploiting a huge electronic energy gain from band gap opening. This instability determines the strength of graphene since it occurs prior to the elastic failure. Such kind of instability may also happen for graphene under inequibiaxial strain as long as the point-like Fermi-surface is retained because a phonon wave vector \mathbf{q} that connects two Dirac points still exists. The anomaly point is not necessarily fixed at K and actually moves away from K in the \mathbf{k} -space due to the change of the symmetry and the subsequent shift of Dirac points in the electronic structure.

Strain states can be categorized into equibiaxial and inequibiaxial strain states, and obviously graphene under equibiaxial strain possesses the same symmetry as pristine graphene. Figure 4.1(a) shows the primitive cell and the first Brillouin zone (BZ) of graphene. Since inequibiaxial strain states are nothing but uniaxial strain states with different lattice constants, systems under inequibiaxial strain has the symmetry of uniaxially strained graphene. Under uniaxial strain, the symmetry of the honeycomb lattice is lowered to D_{2h} , and so does its BZ as in Figure 4.1(b) and (c). Also, the symmetry at the K (or K') point is lowered to C_{2v} due to the symmetry lowering strain, where the two-fold rotational axis is y-axis. Here, strained graphene does not have the three-fold rotational symmetry anymore. The symmetry

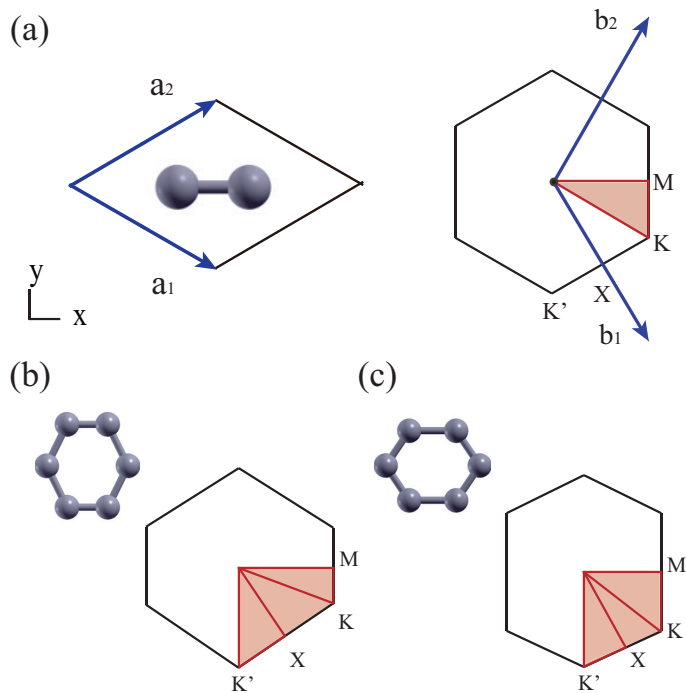


Figure 4.1: (a) Primitive cell and the first Brillouin zone (BZ) of graphene. The irreducible BZ (IBZ) is represented by the shaded area in red. (b),(c) Atomic structures and BZs of graphene under the Z- and A-strain, respectively. The direction of the Z (A)-strain is in parallel with the x (y)-axis. The IBZ is expanded from triangle to trapezoid due to the symmetry lowering strain.

lines wrapping the irreducible BZ (IBZ) are changed as indicated in Figure 4.1 according to the direction of uniaxial strain. The symmetry line along $\overline{\Gamma K'}$ is still equivalent to $\overline{\Gamma(-K')}$ (where $-\mathbf{K}' = \mathbf{K} - \mathbf{b}_1$) owing to the reflection symmetry with respect to x-z and y-z planes, but it is no more equivalent to $\overline{\Gamma K}$ even though phonon frequencies are the same at the high-symmetry points \mathbf{K} and \mathbf{K}' . It is also known that, under uniaxial strain, Dirac points in the electronic structure shift in different manners depending on the strain direction [38]. Therefore, the effect of the inequibiaxial strain state on the BZ symmetry and the electronic structure can be categorized as armchair (A)-strain ($e_x > e_y$) and zigzag (Z)-strain ($e_y > e_x$) states, and the wave vector in phonon spectra that gives rise to the Kohn anomaly falls in different symmetry lines depending on the strain ratio and the direction. (See Figure 4.1(b) and (c)) (Here, we define nominal strains in x and y directions as $e_x = l_x/l_{0x} - 1$ and $e_y = l_y/l_{0y} - 1$, where l_x (l_y) is the length of strained primitive cell in the x (y)-direction, and '0' denotes unstrained (reference) length.)

To see how this Kohn anomaly develops and eventually reaches instability, we investigate the effect of inequibiaxial strain on the phonon band structure along symmetry lines wrapping the irreducible BZ. We compute the phonon spectra of strained graphene using the *ab initio* force constant method [27, 39], where the force constants are generated from the DFT calculation, and all the strain states ap-

plied are represented as (e_x, e_y) .

4.2 Calculation details

All DFT calculations are carried out employing the Vienna *ab initio* simulation package (VASP) [40, 41] with projector augmented wave (PAW) pseudopotentials [42], and exchange-correlation interactions are treated within the local density approximation. The energy cutoff for the plane-wave basis set is set to 375 eV throughout the whole calculation, and the k-point grid of $27 \times 27 \times 1$ is used for the graphene primitive cell. The force constants are generated from supercells of $9 \times 9 \times 1$ times the primitive cell, and the $3 \times 3 \times 1$ k-point mesh is used to maintain the same mesh densities as in the primitive cell. The interlayer distance in the supercell is 15 Å. All internal coordinates are relaxed until the force on each atom is less than 0.01 eV/Å.

4.3 Results and discussion

4.3.1 Symmetry lowering strains and transition of phonon softening points

Figure 4.2 shows the calculated phonon spectra of graphene under various strain states. Here, we assign numbers to identical K (K') points in the BZ to avoid confusion in later discussions. It shows good agreement with previous calculations [32, 43–46] when equibi-

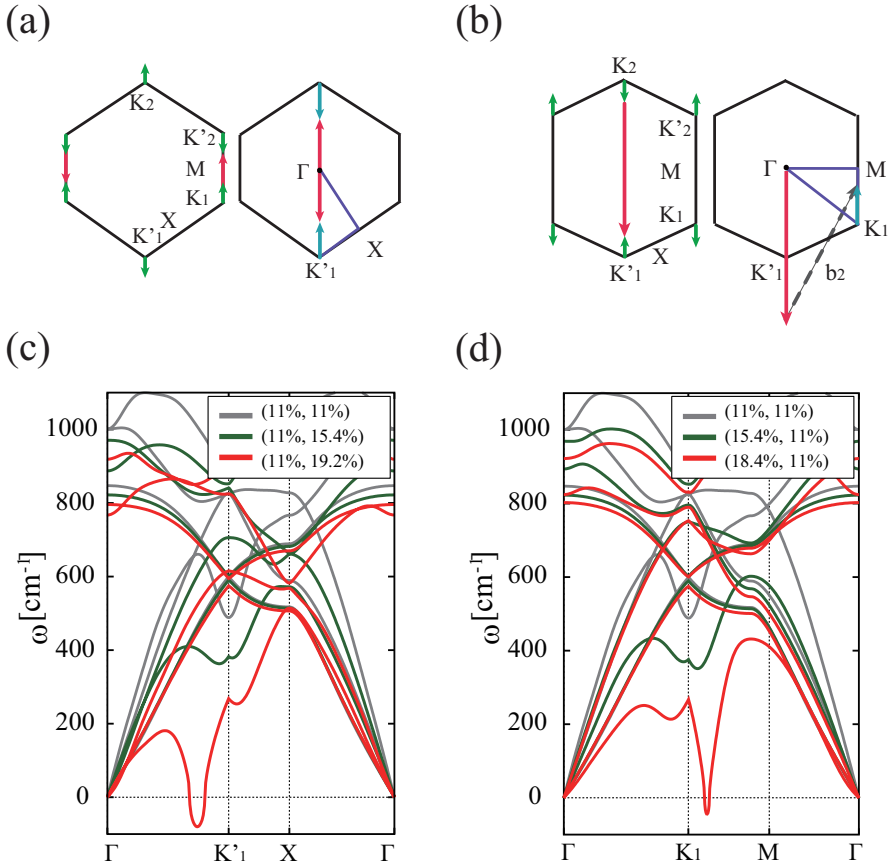


Figure 4.2: (a) BZs of electron (left) and phonon (right), respectively, under the Z-strain and (b) the same for the A-strain. In the left figures of (a) and (b), green arrows represent Dirac points shift, and red arrows are vectors connecting two Dirac points. Blue arrows in the right figures of (a) and (b) represent the positions of the frequency dips (wave vector of the soft phonon) in the phonon dispersion. (c),(d) Phonon band structures under the Z- and A-strain, respectively (plotted along purple lines in (a) and (b)). Different colors indicate different strain configurations (see inset). Phonon softening points gradually move away from K (K') and corresponding phonon frequencies are lowered as the Z (A)-strain increases.

axial strain is applied (i.e., when the lattice constant is increased), as presented in grey curves. As strain increases in the A- or Z-direction from the equibiaxially strained graphene (i.e., the strain ratio deviates from 1), one can see that dips in phonon spectra become deeper and the position of the softening moves away from the K point. Phonon spectra finally become negative (i.e., the phonon mode becomes unstable) at strains of (11%, 19.2%) in Z-strain (Figure 4.2(c)), and of (18.4%, 11%) in A-strain (Figure 4.2(d)), respectively, both prior to elastic failure strain. The elastic failure of pristine graphene happens at (12.8%, 22.3%) (Z-strain) and at (22.0%, 13.2%) (A-strain), respectively, for the cases of the same strain ratios (e_x/e_y) as above. As discussed earlier, the point of the Kohn anomaly shifts under inequibiaxial strain, and Figure 4.2(c) and (d) clearly display how these points move with the increment of uniaxial strain. In Figure 4.2, the Dirac cone moves from the high-symmetry point K to a point on the symmetry line along \overline{KM} or \overline{KT} under Z- or A-strain, respectively, as strain increases. The changed positions of Dirac cones are indicated with green arrows. As a result, the lengths of vectors connecting Dirac points (red arrows) decrease with respect to the lengths of $\overline{\Gamma K}$ and $2\overline{\Gamma K}$ for the Z- and A-strain cases, respectively. In other words, the position of phonon dips gradually approaches Γ from K (M from K') as Z (A)-strain increases, and the traces of the dip are represented by blue arrows. We carry out the same calculation with a 2% increment

in the lattice constant in each step from 1% to 13% in order to reveal how this phenomenon is manifested as a function of strain. By applying Z-strain ($e_y > e_x$) and A-strain ($e_x > e_y$) to graphene of different lattice constants, we find onset strains for the phonon instability. Results show that under wide range of strain states (except when the strain ratio e_y/e_x is less than ~ 0.25), the phonon instability occurs prior to the elastic failure. These phonon instabilities, however, cannot be resolved by K-cell calculations that had been done in previous research [32] because phonon modes getting instabilities away from K-point require larger cell than K-cell.

4.3.2 Crossover between two phonon instabilities

Interestingly, we find that there is a different type of phonon softening occurring near Γ point (Γ -instability in Figure 4.3(a), right figure). This phonon softening is originated from neither the inter-valley interaction between two Dirac points nor the intra-valley interaction, implying that this softening is not associated with the Kohn anomaly at K or Γ . To distinguish this instability from the Kohn anomaly-derived phonon instability (K-anomaly) mentioned before, we henceforth call it as “near Γ -softening”. Especially, this near Γ -softening comes prior to the K-anomaly when the strain ratio e_y/e_x is less than ~ 0.48 .

In Figure 4.3(a) and (b), we plot selected band structures that ex-

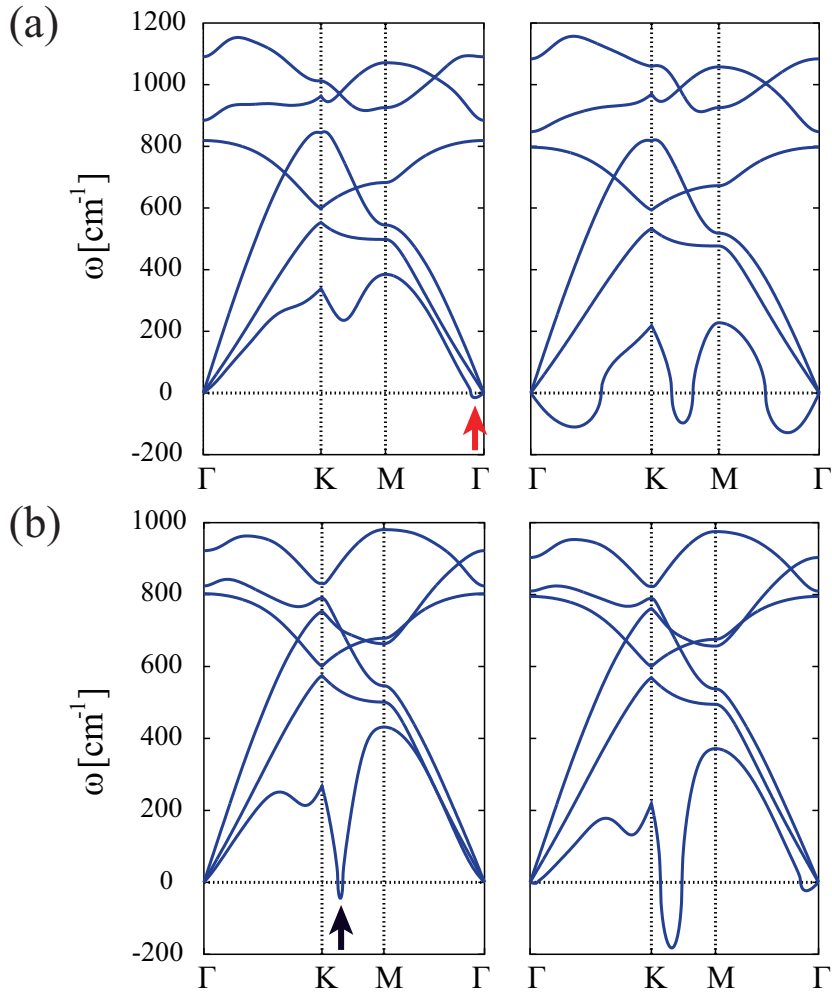


Figure 4.3: Crossover between the near Γ -softening and the K-anomaly. (a) Phonon band structures at $(e_x, e_y) = (0.193, 0.05)$ and $(0.218, 0.05)$ for left and right figures, respectively. The near Γ -softening (red arrow) occurs earlier than the K-anomaly. (b) Phonon band structures at $(e_x, e_y) = (0.184, 0.11)$ and $(0.194, 0.11)$ for left and right figures, respectively. The K-anomaly (black arrow) occurs before the near Γ -softening.

hibit the crossover between the near Γ -softening and the K-anomaly. For the A-strain case, the K-anomaly point moves from K toward M since the vector connecting two Dirac points is shortened from $2|\overrightarrow{\Gamma K'_1}| (= |\overrightarrow{\Gamma K'_1} - \mathbf{b}_2|)$ to $|\overrightarrow{\Gamma K'_1}| + |\overrightarrow{MK'_1}|$ in magnitude, and the phonon instabilities at K and near Γ are easily distinguishable. (See Figure 4.2(a), (b).) $\overrightarrow{\Gamma K'_1}$ is an equivalent vector to $2\overrightarrow{\Gamma K'_1}$ shifted (by \mathbf{b}_2) into the first Brillouin zone, and likewise for $\overrightarrow{\Gamma M}$. In contrast, for the Z-strain case, the shortest length of the line segment between K and K' ($|\overrightarrow{K_1 K'_2}|$) that is aligned in the y-direction becomes shorter than $|\overrightarrow{\Gamma K'_2}|$ as the Z-strain increases while two Dirac points initially located at K and K' approach each other as well. Both of them make the K-anomaly point move from K toward Γ when strain ratio e_x/e_y approaches zero. Therefore, the K-anomaly and the near Γ -softening points get close and are not clearly separable when e_x/e_y is small. Considering both the K-anomaly and the near Γ -softening, the strain states can be separated into two regions according to whether the K-anomaly is followed by the near Γ -softening or vice versa. It is noted that the system acquires the phonon instability prior to the elastic failure (thus releasing the stress as much as possible) under wide range of strain states except when the strain ratio e_y/e_x is less than ~ 0.25 .

4.3.3 Phonon instability-driven mechanical failure

So far, we show how the graphene gets phonon instability under tensile strain states, which can cause the Kekule distortion in the case of biaxial strain. Distorted structures originated from phonon instabilities are less symmetric than the hexagonal structure, and this makes uneven stress concentrations. Consequently, it may drive a mechanical failure (bond breaking) when an additional load is applied. However, the phonon instability or the corresponding distortion does not always accompany a mechanical failure, and we need to explore the strength and stability of distorted graphene quantitatively. Since the anomaly point shifts to a less symmetric position from the high-symmetric K-point (Figure 4.2), the supercell size that can sustain relevant structural transitions should be quite large, and the shape also changes for most strain states. This makes the theoretical testing of the graphene strength under various strain ratios quite difficult. We choose six cases that exhibit phonon instability prior to the elastic failure with onset strains (18.4%, 11%), (7%, 20.9%), (13.33%, 20%), (17%, 14.17%), (19.84%, 7%) and (5%, 22.65%), which have soft phonon modes with computationally manageable supercell sizes.

To see how the phonon instability-induced distortion is related to a mechanical failure, we perform strength and stability tests for those cases by applying strain around the onset strains, as shown in Figure

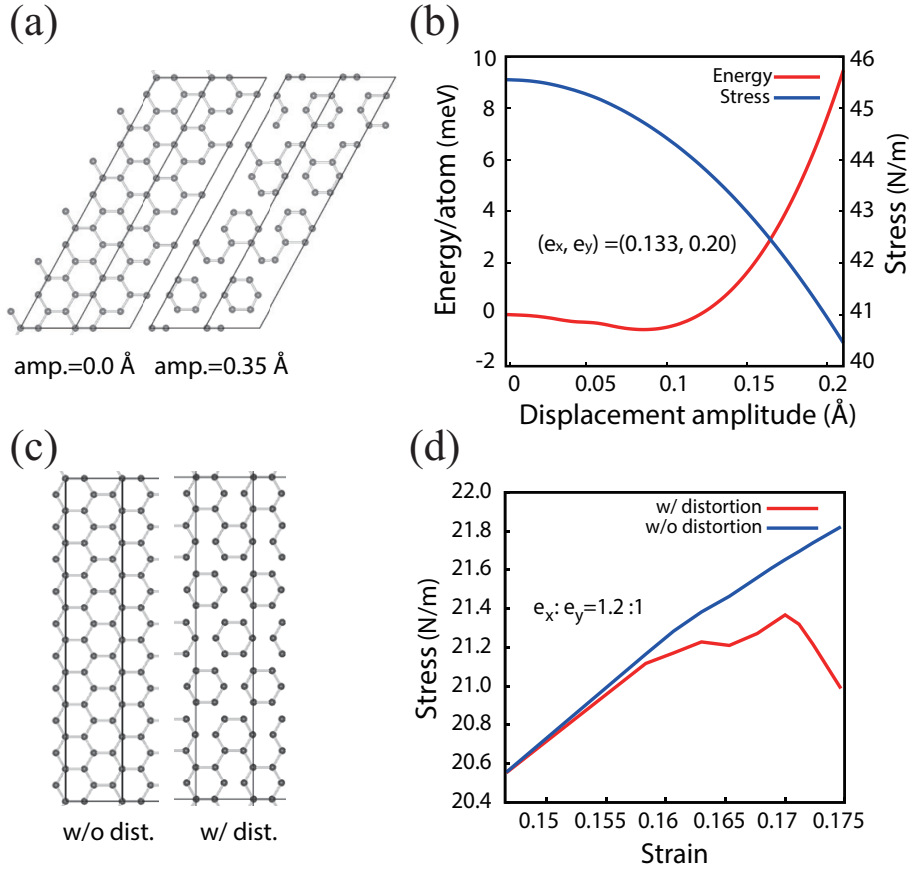


Figure 4.4: (a) Phonon instability-driven distortion occurring at the onset strain of (13.33%, 20%) and (b) the corresponding total energy and stress relation with varying displacement amplitude under the same tensile strain. (c) Phonon instability-driven distortion occurring at the onset strain of (17%, 14.17%) and (d) the stress-strain relation above the onset strain.

4.4. All the systems are confirmed to be distorted and stabilized at the onset strain of phonon instability through the total energy calculations for phonon modes of varying amplitudes. The structural distortion according to the phonon instability occurring at the onset strain of (13.33%, 20%) is shown in Figure 4.4(a), where the phonon amplitude is exaggerated to show the distorted structure clearly. The corresponding total energy with varying phonon amplitude is shown in Figure 4.4(b), where the total energy has a minimum value at a finite displacement amplitude. This structural distortion is accompanied by stress releasing process, i.e., a distorted structure is of less stress than undistorted graphene at the same strain. The distorted structure in Figure 4.4(c) is corresponding to the phonon instability occurring at the onset strain of (17%, 14.17%) and undistorted graphene is under the same strain, on which we apply additional strain. When more tensile strain is applied to the distorted structure, the stress decreases while that of undistorted one increases as shown in Figure 4.4(d), signaling the mechanical failure of graphene. These results indicate the graphene structure is distorted in a way that is commensurate with the soft phonon mode when the strain reaches the onset strain for the phonon instability, and this structural phase transition is responsible for the mechanical failure of graphene prior to the elastic failure.

In Figure 4.5, the distorted structures of three representative cases are presented for detailed discussions on the characteristic of each

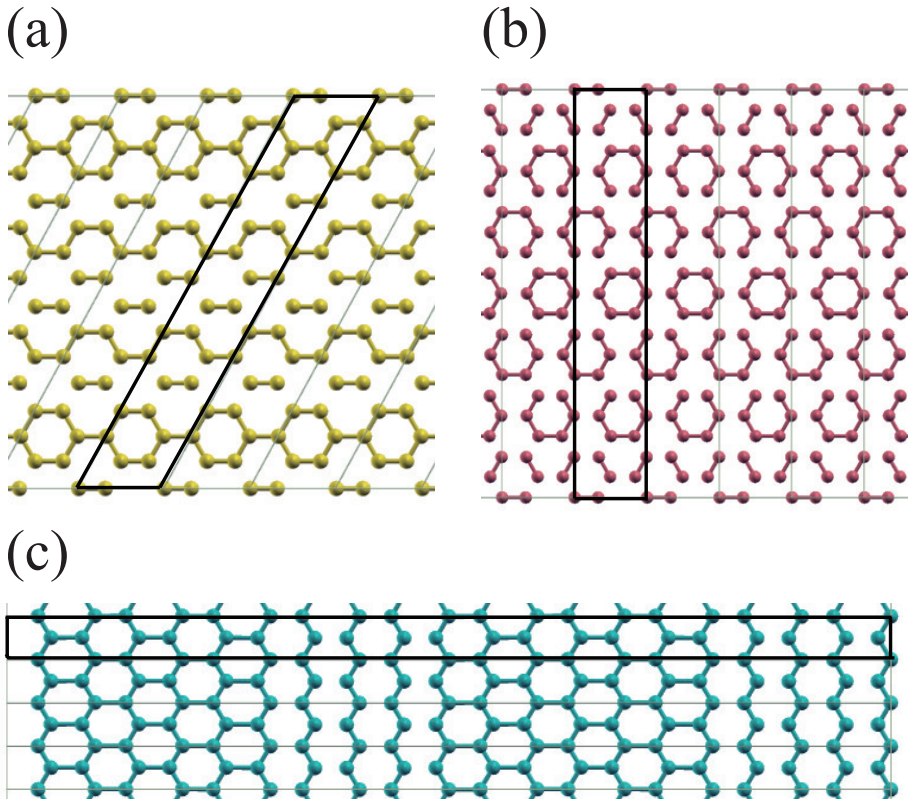


Figure 4.5: (a),(b) Distorted structures induced by the K-anomalies under a Z-strain (13.33%, 20%) and an A-strain (17%, 14.17%), respectively. (c) Distorted structure induced by the near Γ -softening under an A-strain (19.84%, 7%). The K-anomaly induced structures show local hexagonal clustering, while the near Γ -softening induces bond elongation along one direction.

phonon mode: the K-anomaly under the Z-strain (13.33%, 20%), and the A-strain (17%, 14.17%), and the near Γ -softening under the A-strain (19.84%, 7%). An interesting feature induced by the K-anomaly is that the resulting structure consists of hexagon-like closed shapes with slightly different sizes analogous to the Kekule distortion under the biaxial strain. Displacements of two atoms in a primitive cell are circular motions [47] in opposite directions with finite phase difference. On the contrary, the structure induced by the near Γ -softening shows no definite locally closed movements but rather a long-wavelength sinusoidal pattern as a whole, resembling a wave of condensation and rarefaction. We can observe two characteristic features for this mode. First, relative motions of two basis atoms in the primitive cell are nearly in phase for this phonon mode at instability. Second, the corresponding wave vector around Γ is too small to cause enough phase difference between adjacent cells. Therefore, the resultant displacement pattern cannot make a locally closed shape. Rather, the resultant structure is stretched in one direction and the Γ -derived mode has a long-wave nature as shown in Figure 4.5(c), where finite regions with long and short bond length appear alternatively in the direction of applied strain.

4.4 Conclusion

In summary, we show how the phonon softening develops as the tensile strain changes by explicitly calculating the evolution of dips in the phonon spectra. We find that two different types of phonon instability dictate the failure of graphene as they acquire negative frequencies prior to elastic failure. Our research shows not only the intriguing relationship between the ideal strength and strain states but also how deformation of graphene affects electronic structures and corresponding phonon spectra.

Chapter 5

Investigation of graphene/hexagonal boron nitride double layer in regard to an STM experiment

The intrinsic electron mobility of graphene exceeds that of any other semiconductor, however, the extrinsic effects from substrate may affect the electronic properties of graphene in practice. It is critical to have energy band gap and retain high electron mobility to reach the ultimate goal of electronic device application of graphene. In this chapter, we introduce the recent related issues and present the results of experimental and theoretical studies performed on epitaxially grown graphene on hexagonal boron nitride monolayer.

5.1 Introduction

Since its first successful isolation, graphene has been a candidate material for future signal-switching devices with spin-sensitive transport [48]. However, the on-off ratio of the fabricated switching devices is quite low because of the semimetallic nature of graphene, which originates from massless Dirac-fermion dispersion [49]. It was

suggested that a band gap can be produced if two different local potentials are applied to A and B sites of graphene, which can be understood in terms of a Dirac-fermion dispersion with a mass term originated from the broken sublattice symmetry [48]. While the A, B sublattice symmetry is not broken by external electric field in monolayer graphene, it can be broken in bilayer graphene [50]. A bilayer device can be useful because the band gap is tunable when electric fields are applied to the top and bottom layers independently. Alternatively, a similar device can be produced by replacing the bottom layer with hexagonal boron nitride (*h*-BN) monolayer [51–53], which is isostructural to graphene with about 1.8% of lattice mismatch. This can be realized by epitaxial growth or mechanical placement of graphene on *h*-BN monolayer. In graphene on *h*-BN sheet, it has been found that the valley degree of freedom remains intact while graphene has nonzero band mass [54, 55]. Thus, most of the electronic and transport characteristics in free-standing graphene are preserved in graphene on *h*-BN sheet. For example, sharp edge states should be present in graphene nano ribbon (GNR) with zigzag edge termination. In zigzag GNR (ZGNR), the tight-binding calculation predict a degenerate flat band at the Fermi level from $2/3k_{\Gamma X}$ to zone boundary in momentum space. When the spin degree of freedom is factored in, however, antiferromagnetic spin configuration on the honeycomb lattice (a bipartite lattice) becomes the ground state and

it develops band gap [56]. The corresponding edge state, of which the peak height decreases with increasing width of the ZGNR, decays spatially away from the edge with a finite decay length if there is no corresponding bulk state [57]. If there is a corresponding bulk state, however, this edge state may merge with the bulk state, which is called an edge resonance in analogy to surface state and surface resonance.

Meanwhile, the choice of substrate is essential for the sake of the high electron mobility of graphene. The remarkable intrinsic electron mobility of graphene is degraded considerably on conventional substrates such as SiO_2 due to the charge trapping by dangling bonds and extrinsic scattering by surface phonon [6]. *h*-BN has been suggested as an ideal substrate owing to its appealing aspects; it is a large band gap insulator with atomically smooth surface, which is relatively free of dangling bonds and charge traps. Indeed, it has been shown that the mobility of the charge carriers in graphene adsorbed on *h*-BN is comparable to that of suspended graphene at low temperatures [58]. At room temperature, the electron mobility of graphene on *h*-BN is even an order of magnitude higher than that of suspended graphene because the van der Waals interaction between two layers suppresses the thermal ripples of graphene [59]. Besides, there have been issues on the effect of metal substrates on measuring intrinsic properties of graphene. Both theory and experiment have shown that unsaturated

σ -orbitals at graphene edge bind to metal substrate atoms and the edge state predicted in free-standing graphene may be substantially reduced or even absent in graphene on metal substrates [60, 61]. The observed edge states may be mixed with the substrate Au(111) states that leak out of graphene layer [56]. Moreover, various energy gaps of 0.2-0.3 eV have been reported in a ZGNR drop-cast on Au(111) [62], monolayer graphene epitaxially grown on Cu/Ir(111) [63], and bilayer graphene epitaxially grown on Ru(0001) [64]. Theoretically, this band gap opening can be explained by the band hybridization of the metal substrate and graphene [63]. It can be inferred from the aforementioned studies that if we measure electronic properties of graphene directly contacting to metallic substrates, the metallic states decay through the graphene near the Fermi level seriously as prohibiting the measurement of the intrinsic properties of graphene.

In a recent experiment conducted at Kuk's group [65], they investigated electronic properties of graphene epitaxially grown on *h*-BN monolayer by using scanning tunneling spectroscopy (STS). Scanning tunneling microscopy (STM) is an ideal tool for imaging the local geometric structure and measuring the local electronic structure in STS mode. In the experiment, graphene nano islands (GNIs) were epitaxially grown on a likewise epitaxially grown *h*-BN monolayer on Cu(111) surface. Most of the graphene layers were grown on the exposed Cu substrate, while some were grown on *h*-BN layer. Grown

GNIIs were sparse but they were clean without any hint of impurities. There is an experimental way to identify sample, which is observing a Moiré pattern that appears when two layers with angle misalignment or with lattice mismatch are overlapped, but it is an indirect approach. Theoretically, however, we can directly identify the sample by DFT calculations. In regard to the experiment, we do theoretical study on electronic properties of graphene/*h*-BN double layer. First, we perform STM simulation to identify graphene/*h*-BN double layer sample measured in the experiment. Second, we investigate the STS results of the zigzag edge localized state by model calculations.

5.2 Calculation details

We carry out theoretical studies concerning experimental STM and STS data. In regard to an STM image of the epitaxially grown graphene on the *h*-BN sheet, density functional theory (DFT) calculations are performed within the generalized gradient approximation (GGA) using the Vienna *ab initio* simulation package (VASP) [40, 41] with projector augmented wave (PAW) potentials [42]. The energy cutoff for the plane-wave basis set is set to 400 eV and the k-point grid of $27 \times 27 \times 1$ is used throughout the whole calculations. To investigate the effect of substrates on STM experiments several model structures are considered, that is graphene/Cu(111), graphene/*h*-BN/Cu(111), and

h -BN/Cu(111). Among the considered six atomic-layers of copper, the coordinates of bottom three layers are fixed as the bulk values during the geometry optimizations. All other internal coordinates are optimized until the Hellman–Feynman force acting on each atom is less than 0.02 eV/Å. Since conventional density functionals lack the ability to describe the van der Waals interactions, which is important to describe the interaction between graphene and h -BN sheet, the semi-empirical correction is added through Grimme’s method; it is the so-called GGA-D2 method. From the calculated charge density of each system around Fermi energy we perform STM simulations, where charge densities are integrated from $E_{Fermi} - 0.05$ eV to E_{Fermi} and averaged within a circle of radius 1 Å at a given height considering the lateral resolution of STM of 2 Å. For the STM tip the s-wave-tip model is employed [66]. In addition to the DFT calculations, we also perform tight-binding calculations with the Hubbard model Hamiltonian for ZGNRs with various widths (3.4 to 34 nm) to reproduce STS data, which is solved in a mean-field approach. In the text, n-ZGNR denotes n zigzag chains of carbon atoms connected in parallel. The ratio of the on-site repulsive interaction U to the hopping parameter t in the model Hamiltonian is fitted to the measured energy gap, where a hopping parameter of $t = -2.88$ eV for ideal graphene is employed. The effective wave vector k , which is adapted to the observed decay length of the edge state, is obtained from the analytic

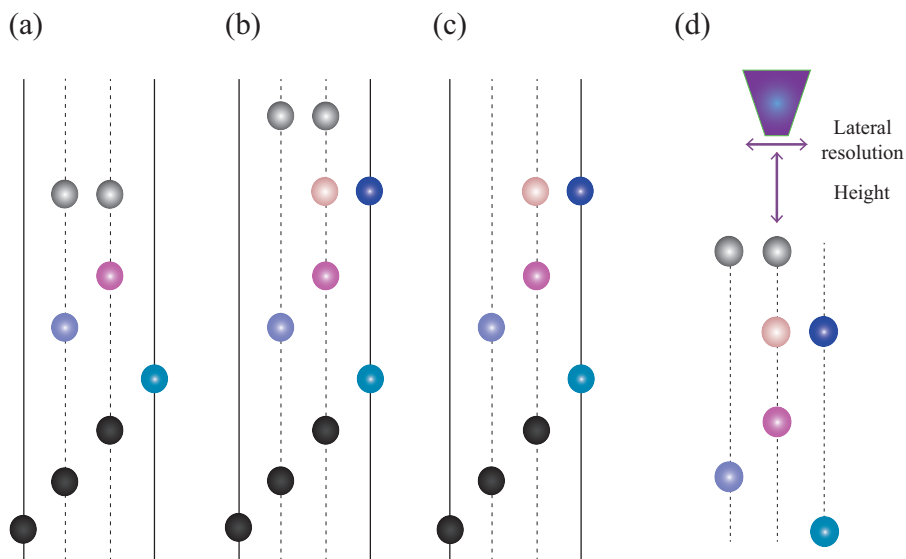


Figure 5.1: Atomic configurations of (a) graphene monolayer, (b) graphene/*h*-BN double layer, and (c) *h*-BN monolayer over six atomic-layer of Cu(111) substrate for STM simulations. Here, we explicitly consider various substrates in the calculations. STM simulation is schematically drawn in (d), where a purple trapezoid represents the STM tip.

solution for the states localized at the zigzag edge of semi-infinite graphene [57].

5.3 Results and discussion

5.3.1 Effect of substrates on STM simulation

While theoretical predictions have been usually made on free-standing graphene, most STM studies have been performed on epitaxially grown or drop-cast graphene flakes on metal substrates. To include the effect

of substrates, we perform DFT calculations for the chosen model systems, which are shown in Figure 5.1(a)-(c). For comparison, we consider three configurations with different substrates; these are graphene monolayer, graphene/*h*-BN double layer, and *h*-BN monolayer over six atomic-layer of Cu(111) substrate, respectively. For all cases, atoms belonging to bottom three layers of copper substrate are fixed during the geometry optimizations to mimic the semi-infinite copper substrate. Figure 5.1(d) is the schematic description of the STM simulation performed in this study.

The simulation results are shown in Figure 5.2(a)-(c), which exhibit the limitation of the STM measurements on graphene directly contacting with the metallic substrate. They are calculated in-plane charge densities of graphene/Cu(111), graphene/*h*-BN/Cu(111), and *h*-BN/Cu(111) systems, respectively. Figure 5.2(b) is calculated at 3 Å away from the outermost layer, and others are calculated at 4 Å away from the layer. We find that charge densities from hybridized C and Cu atoms seem to be dominant at 3 Å away, but the contribution from Cu atoms are still big at 4 Å away from the surface (only 4 Å case is shown in Figure 5.2(a)). On top of graphene epitaxially stacked on *h*-BN monolayer, the contribution from copper substrate is negligible and charge densities are mainly from graphene, as shown in Figure 5.2(b). The huge difference between simulated images with and without *h*-BN makes it clear that metallic substrates can affect the

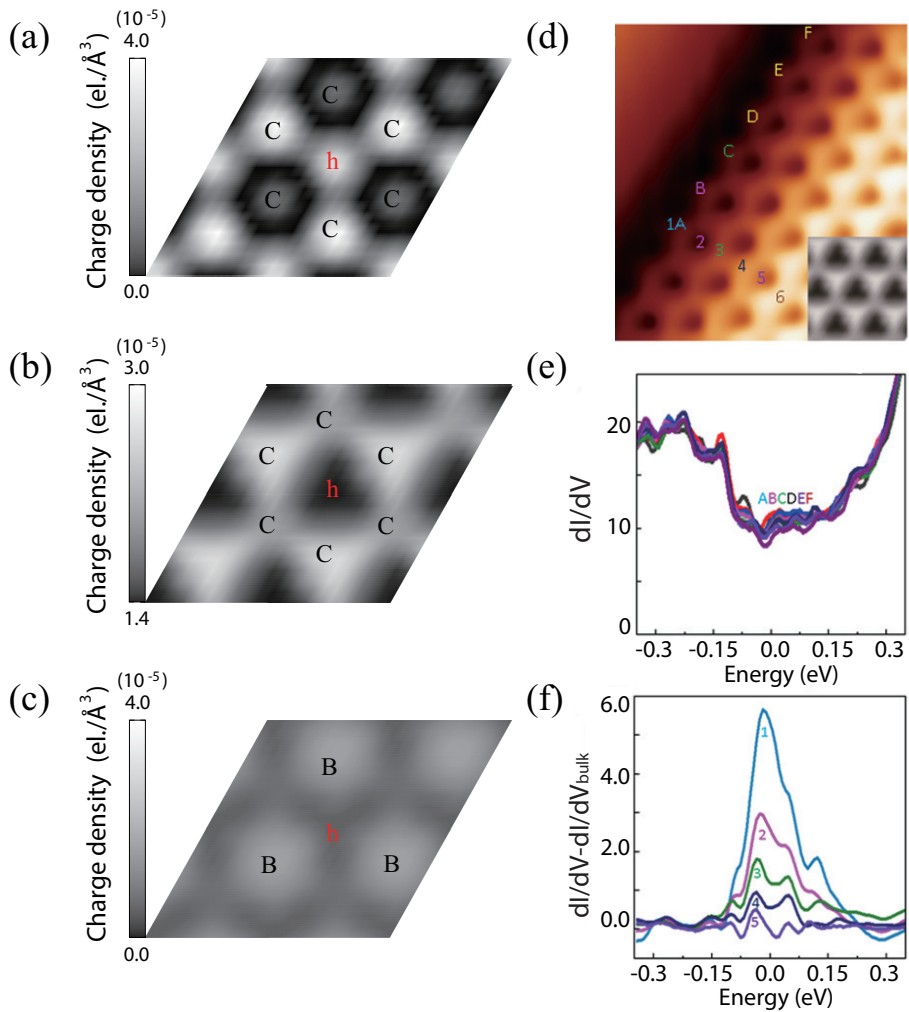


Figure 5.2: Calculated charge densities of (a) graphene on Cu(111) at 4 \AA away, (b) graphene on *h*-BN/Cu(111) at 3 \AA away, and (c) *h*-BN on Cu(111) at 4 \AA away, where h denotes the center of a hexagon. (d) $(1.6 \times 1.6) \text{ nm}^2$ STM topography of graphene monolayer on *h*-BN. A simulated image is shown in the bottom right corner. (e) Tunneling spectra along the zigzag edge at locations A, B, C, D, E, and F in (d). These spectra overlap nicely, showing reproducibility. (f) Difference spectra, dI/dV subtracted from the bulk dI/dV , obtained at locations 1, 2, 3, 4, 5, and 6 in (d).

measured electronic properties of graphene and the usage of an insulating film such as *h*-BN between graphene and metallic substrates is required. In addition, the simulated image of graphene/*h*-BN double layer on Cu(111) (Figure 5.2(b)) shows remarkable resemblance to the measured image in Figure 5.2(d). Here, an inset in Figure 5.2(d) is same with Figure 5.2(b). Therefore, we can identify that the measured part of the sample is indeed graphene/*h*-BN double layer on Cu(111) substrate. Figure 5.2(d) shows a close-up view of a zigzag edge. The curved feature at the edges is due to a finite curvature (≈ 1 nm) of the tunneling tip used to obtain this STM image. The zigzag edge looks perfect without a single defect or reconstruction, up to tens of nanometer. The identity of grown layers can be confirmed by the STS spectra as shown in Figure 5.2(e), which shows the measured tunneling spectra at six equivalent carbon sites along the edge. The spectra overlap nicely with little deviation. The measured local density of states (LDOS) near the Fermi level decreases with increasing distance from the edge, which is proportional to dI/dV in STS. Figure 5.2(f) shows the dI/dV , the first derivative of the tunneling current, subtracted from the bulk dI/dV . These difference spectra clearly show the existence of the edge state at this zigzag edge, where the decay of the edge state is nearly exponential with a decay length of ≈ 2.8 Å. A gap-like feature between two peaks is visible near the Fermi level. The size of the gap does not vary with distance from the edge

of the bulk stripe, and the peak-to-peak energy gap is estimated to be $\approx (0.09 \pm 0.01)$ eV.

To clarify the limitation of previous studies as well as to find out the role of *h*-BN monolayer, we make a further investigation. First, we calculate density of states of the aforementioned three systems projected on carbon p-orbital, copper s-orbital, and boron p-orbital near Fermi energy, which are shown in Figure 5.3(a)-(c). Except the state from boron, those from carbon and copper exist near Fermi energy. If we compare Figure 5.3(a) and (b), we can see that carbon p-orbital, presented in blue dotted line, moves downwards when the *h*-BN is absent, which represents the charge transfer from copper to graphene. We choose two energy ranges to integrate charge densities, one is around carbon p-orbital peak and the other is around copper s-orbital peak. Those peak positions are marked in Figure 5.3(a)-(c), and electronic states in the range of ± 25 meV of the marked peaks are integrated. As a next step, we calculate averaged charge densities for varying height, in the surface normal direction at chosen two (*x,y*) positions marked in Figure 5.2(a)-(c). One is abbreviated by *c* when the position is on top of C, and the other is abbreviated by *h* when that is on top of a hexagonal center of graphene, which is on top of N in the case of *h*-BN monolayer on Cu(111). The decaying patterns of charge densities are shown in Figure 5.3(d)-(f). In Figure 5.3(d), copper s-orbital dominant state decays slower than carbon p-orbital dom-

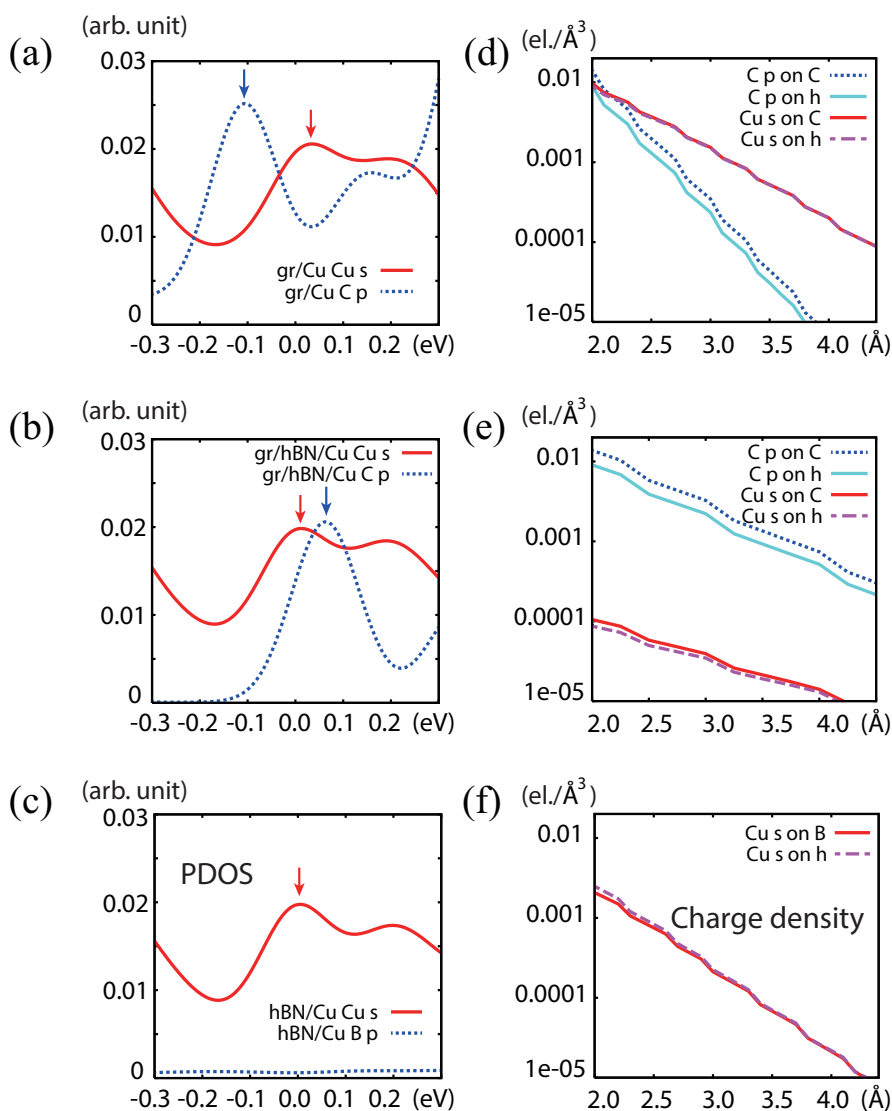


Figure 5.3: Projected density of states onto (a) C p-orbital, (b) Cu s-orbital, and (c) B p-orbital near Fermi energy, respectively. Calculated charge densities in the direction of surface normal are shown in (d) for the marked states in (a), (e) for those in (b), and (f) for those in (c), in log scale. Electronic states in the range of ± 25 meV of marked peaks are integrated for calculating charge densities. Without insulating *h*-BN layer, Cu s-orbital dominant state decays very slowly showing its tail above the graphene layer in (d).

inant state, so it leaks out of the graphene. When h -BN sheet is placed between graphene and Cu(111) (see Figure 5.3(e)), however, the copper s-orbital dominant state decays much faster than carbon p-orbital dominant state. If we compare the Figure 5.3(d) and (f), the copper s-orbital dominant state decays much faster when copper substrate is covered with insulating h -BN monolayer. Thus, we can conclude that the role of h -BN monolayer is not just a spacer but also a dielectric that prevent charge transfer from copper substrate to graphene. In addition, due to the absence of states in the interested energy range, h -BN hardly hybridizes with the states of metallic substrate and avoids metallic charge leakage through it considerably. Hence, if graphene layer is grown on a monolayer-thick insulating layer grown on a metal substrate, it would be an ideal sample to study the near-intrinsic nature of graphene edge states.

5.3.2 Study of localized states at graphene zigzag edge

We investigate on the measured localized state at a zigzag-edged graphene flake on h -BN monolayer, which is shown in Figure 5.2(f). It is known that this edge state should be noticeable in graphene nano islands (GNIs) with a relatively long zigzag edge [67]. In fact, the length of the clean zigzag edge is longer than tens of nanometer, so we model the GNI on h -BN monolayer as ZGNR on h -BN monolayer. Furthermore, previous studies have shown the substrate-induced band

gap renormalization in semiconducting carbon nanotubes [68], and graphene nanoribbons with armchair and zigzag edges [69] supported on *h*-BN monolayer. The reduction of band gap, though it is slight, has been attributed to a more effective screening of the Coulomb interaction in the considered systems by the *h*-BN substrate compared to the screening by the vacuum in free-standing cases. Aside from slightly renormalized band gap, the low-energy electronic structures of the systems are nearly unaffected. The results of the previous studies indicate that the major effect of *h*-BN to the low-energy states of the whole system is reducing the original band gap of the carbon-based system, whose effect is clearly different from that of metal substrates [56, 60–64]. This band gap is proportional to the strength of the on-site repulsive interaction in the Hubbard model Hamiltonian for ZGNR. Consequently, we may consider that the primary effect of *h*-BN in our system is renormalizing the on-site repulsive interaction in the low-energy effective Hamiltonian for ZGNR and reducing the band gap, mostly because *h*-BN sheet is a dielectric material with a huge band gap. Thus, we investigate the measured edge state by solving the effective Hamiltonian. We should note that the π -orbital Hubbard model theory is adopted here because it is broadly consistent with DFT calculations when parameter U is appropriately chosen [70].

The calculated band gap varies as a function of the crystal mo-

momentum, where by band gap we mean the energy difference between the lowest conduction band and the highest valence band at a given k point. By comparing the measured decay length and the analytic solution of the edge state for semi-infinite graphene [57], we can extract an effective momentum k (k_{eff}) of the decaying state coupled with the probing tip, that is $0.81k_{\Gamma X}$. (The measured k_{eff} may vary for different probing tips.) From the known effective momentum, we can estimate the energy gap observed at the zigzag edge. We calculate two band structures with the consideration of on-site repulsive interaction only at the edges, which shows a metallic edge state (the left panel in Figure 5.4(a)) and at all carbon sites, which shows a semi-conducting edge state (the right panel in Figure 5.4(a)) for a very long ZGNR. For shorter ZGNRs, however, we can retrieve a band gap in either case. The calculated LDOS is shown in Figure 5.4(b), where the color codes are consistent with the STS data (see Figure 5.2(f)). By controlling U over t ratio in the model Hamiltonian, we find that the $|U/t|$ value of 0.1 reproduces well the experimental LDOS, especially the interval between two peaks near Fermi energy. The calculated gap at k_{eff} does not change much depending on the ribbon width.

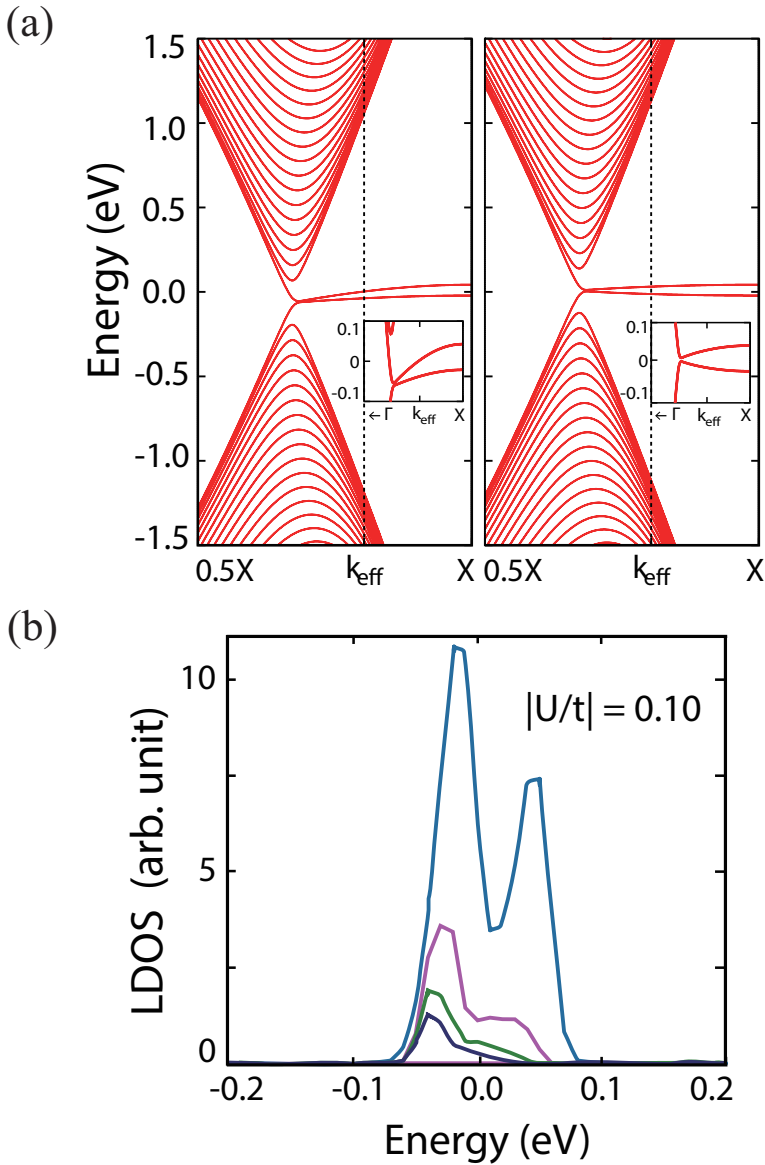


Figure 5.4: (a) Tight-binding band structures of 100-ZGNR. Depending on whether on-site Coulomb repulsion terms are considered only at the zigzag edges or at all carbon sites, the edge state becomes conducting (the left panel) or semiconducting (the right panel). (b) Calculated LDOS at the zigzag edge, which reproduces well STS data measured on the zigzag edge in Figure 5.2(f).

5.4 Conclusion

In summary, we introduce that graphene/*h*-BN double layer can be a candidate material for future electronic devices because it has energy band gap and retains high electron mobility even at room temperature. We show that the measured sample is indeed graphene/*h*-BN double layer on Cu(111) substrate by STM simulation based on DFT calculations. We demonstrate the limitation of STM measurements on graphene directly contacting with metal substrates. Moreover, we reveal the role of *h*-BN monolayer between graphene and a metal substrate by showing the differences in the projected density of states and decaying patterns of charge densities for the chosen systems. We also investigate the zigzag edge localized state of graphene on *h*-BN monolayer with the π -orbital Hubbard model Hamiltonian by considering the system as a ZGNR. From this study, we can not only support the measured results in STM and STS experiments but also clarify the role of *h*-BN monolayer and the advantage of using it as a substrate in measuring intrinsic properties of graphene.

Chapter 6

Summary and perspectives

In summary, we have investigated the mechanical and electronic properties of graphene under extrinsic conditions based on first-principles calculations. First, we elaborate on the basic properties of graphene and effective theoretical models to describe low-energy physics of graphene. We also have introduced density functional theory and computational methods employed in this thesis. In the first part of the following chapters, we have studied the phonon softening and mechanical failure of graphene under the externally applied mechanical stress in general directions. We want to note that the present study have assumed the uniform deformation of graphene. Considering that actual experiments can involve non-uniformity such as strain gradients, a further study is required to see how non-uniform deformation affects the strength of graphene. In the remaining part, we have studied the electronic properties of graphene under the effect of metallic and insulating substrates in regard to a scanning tunneling microscopy experiment. We may suggest that the proper choice of substrate can prevent a possible substrate-induced degradation of electronic properties of graphene. In addition, we have a chance to improve intrinsic

properties of graphene such as introducing a band gap, with the substrate. The studies presented here may be applied to other rising two-dimensional materials and provide help for a deeper understanding of their properties under extrinsic conditions.

Bibliography

- [1] A. K. Geim and K. S. Novoselov. The rise of graphene. *Nat. Mater.*, 6:183–191, 2007.
- [2] K. S. Novoselov, A. K. Geim, S. V. Morozov, D. Jiang, Y. Zhang, S. V. Dubonos, I. V. Grigorieva, and A. A. Firsov. Electric field effect in atomically thin carbon films. *Science*, 306:666–669, 2004.
- [3] N. D. Mermin. Crystalline order in two dimensions. *Phys. Rev.*, 176:250–254, 1968.
- [4] C. Lee, X. Wei, J. W. Kysar, and J. Hone. Measurement of the elastic properties and intrinsic strength of monolayer graphene. *Science*, 321:385–388, 2008.
- [5] F. Schedin, A. K. Geim, S. V. Morozov, E. W. Hill, P. Blake, M. I. Katsnelson, and K. S. Novoselov. Detection of individual gas molecules adsorbed on graphene. *Nat. Mater.*, 6:652–655, 2007.
- [6] J.-H. Chen, C. Jang, S. Xiao, M. Ishigami, and M. S. Fuhrer. Intrinsic and extrinsic performance limits of graphene devices on SiO₂. *Nat. Nanotechnol.*, 3:206–209, 2008.

- [7] G. W. Semenoff. Condensed-matter simulation of a three-dimensional anomaly. *Phys. Rev. Lett.*, 53:2449–2452, 1984.
- [8] E. Fradkin. Critical behavior of disordered degenerate semiconductors. II. spectrum and transport properties in mean-field theory. *Phys. Rev. B*, 33:3263–3268, 1986.
- [9] F. D. M. Haldane. Model for a quantum hall effect without landau levels: Condensed-matter realization of the "parity anomaly". *Phys. Rev. Lett.*, 61:2015–2018, 1988.
- [10] M. S. Dresselhaus and G. Dresselhaus. Intercalation compounds of graphite. *Advances in Physics*, 51:1–186, 2002.
- [11] C. Berger, Z. Song, X. Li, X. Wu, N. Brown, C. Naud, D. Mayou, T. Li, J. Hass, A. N. Marchenkov, E. H. Conrad, P. N. First, and W. A. de Heer. Electronic confinement and coherence in patterned epitaxial graphene. *Science*, 312:1191–1196, 2006.
- [12] S. Stankovich, D. A. Dikin, R. D. Piner, K. A. Kohlhaas, A. Kleinhammes, Y. Jia, Y. Wu, S. T. Nguyen, and R. S. Ruoff. Synthesis of graphene-based nanosheets via chemical reduction of exfoliated graphite oxide. *Carbon*, 45:1558 – 1565, 2007.
- [13] T. Land, T. Michely, R. Behm, J. Hemminger, and G. Comsa. STM investigation of single layer graphite structures produced

- on Pt(111) by hydrocarbon decomposition. *Surface Science*, 264:261 – 270, 1992.
- [14] S. Y. Zhou, D. A. Siegel, A. V. Fedorov, F. E. Gabaly, A. K. Schmid, A. H. C. Neto, D. H. Lee, and A. Lanzara. Origin of the energy bandgap in epitaxial graphene. *Nat. Mater.*, 7:259–260, 2008.
- [15] P. Hohenberg and W. Kohn. Inhomogeneous electron gas. *Phys. Rev.*, 136:B864–B871, 1964.
- [16] W. Kohn. *Highlights in Condensed Matter Theory*. North Holland, Amsterdam, 1985.
- [17] W. Kohn and L. J. Sham. Self-consistent equations including exchange and correlation effects. *Phys. Rev.*, 140:A1133–A1138, 1965.
- [18] D. M. Ceperley and B. J. Alder. Ground state of the electron gas by a stochastic method. *Phys. Rev. Lett.*, 45:566–569, 1980.
- [19] J. P. Perdew, K. Burke, and M. Ernzerhof. Generalized gradient approximation made simple. *Phys. Rev. Lett.*, 77:3865–3868, 1996.
- [20] J. C. Phillips. Energy-band interpolation scheme based on a pseudopotential. *Phys. Rev.*, 112:685–695, 1958.

- [21] J. C. Phillips and L. Kleinman. New method for calculating wave functions in crystals and molecules. *Phys. Rev.*, 116:287–294, 1959.
- [22] L. Kleinman and D. M. Bylander. Efficacious form for model pseudopotentials. *Phys. Rev. Lett.*, 48:1425–1428, 1982.
- [23] P. E. Blöchl. Projector augmented-wave method. *Phys. Rev. B*, 50:17953–17979, 1994.
- [24] C. Rostgaard. The projector augmented-wave method. *arXiv:0910.1921*, 2009.
- [25] S. Grimme. Semiempirical GGA-type density functional constructed with a long-range dispersion correction. *Journal of Computational Chemistry*, 27:1787–1799, 2006.
- [26] G. Kresse, J. Furthmüller, and J. Hafner. Ab initio force constant approach to phonon dispersion relations of diamond and graphite. *Europhysics Letters*, 32:729, 1995.
- [27] K. Parlinski, Z. Q. Li, and Y. Kawazoe. First-principles determination of the soft mode in cubic ZrO_2 . *Phys. Rev. Lett.*, 78:4063–4066, 1997.
- [28] J. R. Greer and W. D. Nix. Nanoscale gold pillars strengthened through dislocation starvation. *Phys. Rev. B*, 73:245410, 2006.

- [29] T. Zhu, J. Li, S. Ogata, and S. Yip. Mechanics of ultra-strength materials. *MRS Bulletin*, 34:167–172, 2009.
- [30] A. A. Griffith. The phenomena of rupture and flow in solids. *Philosophical Transactions of the Royal Society of London A: Mathematical, Physical and Engineering Sciences*, 221:163–198, 1921.
- [31] Q. Zhao, M. B. Nardelli, and J. Bernholc. Ultimate strength of carbon nanotubes: A theoretical study. *Phys. Rev. B*, 65:144105, 2002.
- [32] C. A. Marianetti and H. G. Yevick. Failure mechanisms of graphene under tension. *Phys. Rev. Lett.*, 105:245502, 2010.
- [33] S. J. Woo and Y.-W. Son. Ideal strength of doped graphene. *Phys. Rev. B*, 87:075419, 2013.
- [34] S.-H. Lee, H.-J. Chung, J. Heo, H. Yang, J. Shin, U.-I. Chung, and S. Seo. Band gap opening by two-dimensional manifestation of peierls instability in graphene. *ACS Nano*, 5:2964–2969, 2011.
- [35] P. L. Taylor. Theory of kohn anomalies in the phonon spectra of metals. *Phys. Rev.*, 131:1995–1999, 1963.

- [36] S. Piscanec, M. Lazzeri, F. Mauri, A. C. Ferrari, and J. Robertson. Kohn anomalies and electron-phonon interactions in graphite. *Phys. Rev. Lett.*, 93:185503, 2004.
- [37] C. Chamon. Solitons in carbon nanotubes. *Phys. Rev. B*, 62:2806–2812, 2000.
- [38] S.-M. Choi, S.-H. Jhi, and Y.-W. Son. Effects of strain on electronic properties of graphene. *Phys. Rev. B*, 81:081407, 2010.
- [39] A. Togo, F. Oba, and I. Tanaka. First-principles calculations of the ferroelastic transition between rutile-type and CaCl_2 -type SiO_2 at high pressures. *Phys. Rev. B*, 78:134106, 2008.
- [40] G. Kresse and J. Furthmüller. Efficient iterative schemes for *ab initio* total-energy calculations using a plane-wave basis set. *Phys. Rev. B*, 54:11169–11186, 1996.
- [41] G. Kresse and J. Furthmüller. Efficiency of *ab-initio* total energy calculations for metals and semiconductors using a plane-wave basis set. *Computational Materials Science*, 6:15 – 50, 1996.
- [42] G. Kresse and D. Joubert. From ultrasoft pseudopotentials to the projector augmented-wave method. *Phys. Rev. B*, 59:1758–1775, 1999.

- [43] F. Liu, P. Ming, and J. Li. *Ab initio* calculation of ideal strength and phonon instability of graphene under tension. *Phys. Rev. B*, 76:064120, 2007.
- [44] E. Cadelano, P. L. Palla, S. Giordano, and L. Colombo. Non-linear elasticity of monolayer graphene. *Phys. Rev. Lett.*, 102:235502, 2009.
- [45] A. van de Walle and G. Ceder. The effect of lattice vibrations on substitutional alloy thermodynamics. *Rev. Mod. Phys.*, 74:11–45, 2002.
- [46] O. Dubay and G. Kresse. Accurate density functional calculations for the phonon dispersion relations of graphite layer and carbon nanotubes. *Phys. Rev. B*, 67:035401, 2003.
- [47] J.-A. Yan, W. Y. Ruan, and M. Y. Chou. Phonon dispersions and vibrational properties of monolayer, bilayer, and trilayer graphene: Density-functional perturbation theory. *Phys. Rev. B*, 77:125401, 2008.
- [48] A. H. Castro Neto, F. Guinea, N. M. R. Peres, K. S. Novoselov, and A. K. Geim. The electronic properties of graphene. *Rev. Mod. Phys.*, 81:109–162, 2009.
- [49] F. Xia, D. B. Farmer, Y. ming Lin, and P. Avouris. Graphene field-effect transistors with high on/off current ratio and large

- transport band gap at room temperature. *Nano Letters*, 10:715–718, 2010.
- [50] Y. Zhang, T.-T. Tang, C. Girit, Z. Hao, M. C. Martin, A. Zettl, M. F. Crommie, Y. R. Shen, and F. Wang. Direct observation of a widely tunable bandgap in bilayer graphene. *Nature*, 459:820–823, 2009.
- [51] G. Giovannetti, P. A. Khomyakov, G. Brocks, P. J. Kelly, and J. van den Brink. Substrate-induced band gap in graphene on hexagonal boron nitride: *Ab initio* density functional calculations. *Phys. Rev. B*, 76:073103, 2007.
- [52] J. Jung, A. Raoux, Z. Qiao, and A. H. MacDonald. *Ab initio* theory of moiré superlattice bands in layered two-dimensional materials. *Phys. Rev. B*, 89:205414, 2014.
- [53] M. Bokdam, T. Amlaki, G. Brocks, and P. J. Kelly. Band gaps in incommensurable graphene on hexagonal boron nitride. *Phys. Rev. B*, 89:201404, 2014.
- [54] B. Hunt, J. D. Sanchez-Yamagishi, A. F. Young, M. Yankowitz, B. J. LeRoy, K. Watanabe, T. Taniguchi, P. Moon, M. Koshino, P. Jarillo-Herrero, and R. C. Ashoori. Massive dirac fermions and hofstadter butterfly in a van der waals heterostructure. *Science*, 340:1427–1430, 2013.

- [55] M. Yankowitz, J. Xue, D. Cormode, J. D. Sanchez-Yamagishi, K. Watanabe, T. Taniguchi, P. Jarillo-Herrero, P. Jacquod, and B. J. LeRoy. Emergence of superlattice dirac points in graphene on hexagonal boron nitride. *Nat. Phys.*, 8:382–386, 2012.
- [56] Y.-W. Son, M. L. Cohen, and S. G. Louie. Half-metallic graphene nanoribbons. *Nature*, 444:347–349, 2006.
- [57] M. Fujita, K. Wakabayashi, K. Nakada, and K. Kusakabe. Peculiar localized state at zigzag graphite edge. *Journal of the Physical Society of Japan*, 65:1920–1923, 1996.
- [58] C. R. Dean, A. F. Young, I. Meric, C. Lee, L. Wang, S. Sorgenfrei, K. Watanabe, T. Taniguchi, P. Kim, K. L. Shepard, and J. Hone. Boron nitride substrates for high-quality graphene electronics. *Nat. Nanotechnol.*, 5:722–726, 2010.
- [59] E. V. Castro, H. Ochoa, M. I. Katsnelson, R. V. Gorbachev, D. C. Elias, K. S. Novoselov, A. K. Geim, and F. Guinea. Limits on charge carrier mobility in suspended graphene due to flexural phonons. *Phys. Rev. Lett.*, 105:266601, 2010.
- [60] Y. Li, D. Subramaniam, N. Atodiresei, P. Lazić, V. Caciuc, C. Pauly, A. Georgi, C. Busse, M. Liebmann, S. Blugel, M. Pratzer, M. Morgenstern, and R. Mazzarello. Absence of

- edge states in covalently bonded zigzag edges of graphene on Ir(111). *Advanced Materials*, 25:1967–1972, 2013.
- [61] H. Shu, X. Chen, X. Tao, and F. Ding. Edge structural stability and kinetics of graphene chemical vapor deposition growth. *ACS Nano*, 6:3243–3250, 2012.
- [62] G. Z. Magda, X. Jin, I. Hagymasi, P. Vancso, Z. Osvath, P. Nemes-Incze, C. Hwang, L. P. Biro, and L. Tapasztó. Room-temperature magnetic order on zigzag edges of narrow graphene nanoribbons. *Nature*, 514:608–611, 2014.
- [63] H. Vita, S. Böttcher, K. Horn, E. N. Voloshina, R. E. Ovcharenko, T. Kampen, A. Thissen, and Y. S. Dedkov. Understanding the origin of band gap formation in graphene on metals: graphene on Cu/Ir(111). *Scientific Reports*, 4:5704, 2014.
- [64] E. Sutter, D. P. Acharya, J. T. Sadowski, and P. Sutter. Scanning tunneling microscopy on epitaxial bilayer graphene on ruthenium (0001). *Applied Physics Letters*, 94:133101, 2009.
- [65] B. Hwang. *Properties of CVD-grown graphene/hexagonal boron nitride double-layer : a scanning tunneling microscopy study*. PhD thesis, Seoul National University, 2014.
- [66] J. Tersoff and D. R. Hamann. Theory of the scanning tunneling microscope. *Phys. Rev. B*, 31:805–813, 1985.

- [67] K. Nakada, M. Fujita, G. Dresselhaus, and M. S. Dresselhaus. Edge state in graphene ribbons: Nanometer size effect and edge shape dependence. *Phys. Rev. B*, 54:17954–17961, 1996.
- [68] N. A. Lanzillo, N. Kharche, and S. K. Nayak. Substrate-induced band gap renormalization in semiconducting carbon nanotubes. *Scientific Reports*, 4:3609, 2014.
- [69] X. Jiang, N. Kharche, P. Kohl, T. B. Boykin, G. Klimeck, M. Luisier, P. M. Ajayan, and S. K. Nayak. Giant quasi-particle bandgap modulation in graphene nanoribbons supported on weakly interacting surfaces. *Applied Physics Letters*, 103:133107, 2013.
- [70] J. Jung and A. H. MacDonald. Carrier density and magnetism in graphene zigzag nanoribbons. *Phys. Rev. B*, 79:235433, 2009.

국문 초록

지난 2004년 그래핀이 발견된 이후 이차원 물질 그래핀의 시대가 열렸다. 그래핀은 이론 물리학자와 실험 물리학자 모두에게 흥미진진한 실험의 장이 되어왔는데, 이는 그래핀이 2차원 물질이라는 사실과 더불어 그의 매력적인 물성 때문이다. 많은 이론 연구들이 무한한 격자 구조를 가지는 이상적인 그래핀에 대해 이루어졌는데, 우리가 실제 실험 상황에서 경험하게 되는 것들은 이상적인 그래핀에서 이론적으로 예측되는 성질들과 차이가 있다. 따라서 외부 환경에 의하여 변화된 그래핀의 성질을 예측하는 것은 그래핀의 고유한 성질을 밝히는 것만큼이나 중요하다. 한편, 이러한 고유한 특성으로부터의 차이는 실제 표본에 존재하는 모서리나 경계면, 기판에 의해 가해진 압력, 그리고 기판과의 전자적 섞임 등에 의하여 나타날 수 있다. 실제로 물질을 다룰 때 모서리나 경계면을 피할 수는 없지만 그것들을 정제하고 개선할 여지가 있다. 또한 적절한 기판을 선택함으로써 물성의 저하를 막거나 특정한 상황에서는 오히려 물성을 개선할 수도 있다.

이 논문에서는 이러한 사실들을 염두에 두고 외부 환경 아래에 놓인 그래핀의 역학적 성질과 전자적 성질에 중점을 두었다. 첫 번째 부분에서는 장력이 가해지고 있는 그래핀의 역학적 성질에 대해서 다루었다. 그래핀의 소리알 분산을 구하기 위하여 일반적인 제일 원리 계산과 함께 제일 원리 힘 상수 방법을 이용하였다. 그래핀의 대칭성을 낮추는 장력이 작용할 때 소리알 분산의 콘 아노말리가 나타나는 점이 브릴루앙 영역의 대칭성이 높은 점으로부터 대칭성이 낮은 점으로 이동해 가는데, 이러한

현상은 전자 구조에서 나타나는 디락 점의 이동과 관련지어 이해할 수 있다. 장력에 의해 감소된 소리알의 분산이 광범위한 방향에 걸쳐 불안정해지고, 결국 탄성 파손의 경우보다 더 낮은 장력에서 그래핀이 파손되는 결과를 낳는 것을 보였다. 또한 탄성 파손이 일어나기 전에 그래핀의 파손을 야기하는 두 가지 종류의 소리알 불안정성이 있음을 보였다. 두 번째 부분에서는 훑기 꿰뚫기 실험 결과와 관련하여 켄트 싹기로 기른 그래핀 육각 질화붕소 이중 구조에 대해 다루었다. 먼저 제일 원리 계산에 바탕을 둔 훑기 꿰뚫기 현미경 모의실험을 통하여 실험에서 측정된 표본을 이론적으로 확인하였고, 금속 표면에 직접 접촉하고 있는 그래핀에 대한 훑기 꿰뚫기 실험의 한계를 지적하였다. 또한 육각 질화붕소가 있는 경우와 없는 경우에 대해 원자 오비탈에 투영한 전자 상태 밀도 및 표면에서의 전자 밀도 감소 모양을 비교함으로써 육각 질화붕소의 역할을 분명히 밝혔다. 이와 더불어 육각 질화붕소 위에 놓인 갈지자형 모서리가 잘 발달한 그래핀 나노 조각에서 관측된 모서리 국소 상태를 저에너지 유효 해밀토니안을 통하여 연구하고 실험 결과를 재현했다. 끝으로 이 논문을 요약하고 후속 연구에 대한 전망을 제시하였다.

주요어: 그래핀, 콘 아노말리, 소리알 불안정성, 그래핀 육각 질화붕소 이중구조, 훑기 꿰뚫기 현미경 모의실험, 갈지자형 모서리 그래핀

학번: 2009-20435